Engineering with Computers (2026) 42:194
https://doi.org/10.1007/s00366-026-02433-y

ORIGINAL ARTICLE

FLOWS: a model to simulate water and solutes fluxes in agricultural and environmental systems: 2. Modules for specific applications in water and nutrient management

Antonio Coppola[1] · Angelo Basile[2] · Alessandro Comegna[3] · Caterina Fenu[4] · Anna Concas[4] · Fabio Pili[4] · Shawkat B. M. Hassan[1]

Received: 13 March 2026 / Accepted: 17 September 2026
© The Author(s) 2026

Abstract

This paper is the second of two companion studies. The first paper focused on describing the model FLOWS, theory and the model benchmarking. This paper addresses FLOWS modules on specific applications: irrigation, temperature, organic carbon processes and nutrient transformation and transport in the soil. It also includes applications of FLOWS model in real scenarios. In the irrigation module, FLOWS allows for different scenarios: (1) no irrigation, i.e., only rainfall; (2) irrigation introduced by the user as a top-boundary, temporally variable, input flux; (3) irrigation computed as the daily potential evapotranspiration demand; and (4) irrigation computed by the model. In the latter, FLOWS optimizes irrigation fluxes and schedule according to a criterion based on the average pressure head along a user-specified depth, e.g., the root zone. Since soil temperature influences several soil processes, FLOWS simulates the temperature distribution in depth and time by using a solution to heat flow equations proposed by van Wijk and De Vries. FLOWS simulates fertilizer applications as organic matter (manure and crop residues) or mineral fertilizers. It can either simulate organic matter decomposition with coupled carbon, nitrogen, and phosphorus transformations governed by C:N and C:P ratios or simulate nitrogen transport alone using an empirical mineralization approach independent on organic matter dynamics. Two applications of the model are presented in this paper: (1) analysing the role of spatial variability in soil and vegetation for large-scale irrigation optimization, and (2) monitoring and modelling water and nutrient fluxes from irrigated fields to the surface drainage network. In the first application, FLOWS proved reliable for optimizing irrigation at large scales by accounting for the spatial variability of soil and vegetation properties and by enabling the analysis of the uncertainty associated with progressively overlooking this variability. In the second application, FLOWS was coupled with another physically based model (KWV) founded on kinematic wave theory. FLOWS was used to accurately simulate water, nitrate, and phosphorus fluxes to runoff, which were then routed through the KWV model to produce runoff hydrographs and nutrient concentrations at different sections of the drainage network and at the field outlet.

Keywords Irrigation Optimization · Soil Nutrient Transformation and Transport · Soil Organic Carbon Processes · Water and Contraminant Fluxes to Runoff · Fertilizer Management

✉ Shawkat B. M. Hassan
shawkat.hassan@unibas.it

[1] Department of Chemical and Geological Sciences, University of Cagliari, 09124 Cagliari, Italy

[2] Institute for Mediterranean Agricultural and Forestry Systems, National Research Council, 80055 Portici, NA, Italy

[3] Department of Agricultural, Forestry, Food and Environmental Sciences, University of Basilicata, 85100 Potenza, Italy

[4] Department of Mathematics and Computer Science, University of Cagliari, 09124 Cagliari, Italy

Published online: 06 October 2026

1 Introduction

Several environmental problems are partly or totally related to agricultural activities. The agricultural sector is responsible for most of water consumptions for both irrigation and livestock activities. It is also the main source of diffuse pollution to the surface and groundwater bodies by agrochemicals (pesticides, nutrients, salts, …). Besides, considering that soil organic matter stores significant amounts of carbon, agricultural activities may either attenuate or exacerbate the production of greenhouse gases (GHG), depending on the soil tillage and, in general, on the soil management practices for crop productions. Yet, agriculture may even be the solution to these and other environmental issues, by providing significant environmental ecosystem services, such as regulation of soil and water quality, carbon sequestration, support for biodiversity and cultural services [1].

Quantification of the impacts of agriculture activities on the environment is crucial; on one side, to find practical solutions in terms of technologies and best practices to be adopted to minimise detrimental impacts, on the other side to evaluate the response of solutions to the several national and international directives aiming at ameliorating and protecting the quality of the environment (i.e., 2000/60/EC—Water Framework Directive, 91/676/EC -Nitrate Directive, 128/2009/EC-Pesticide Directive, Zero Pollution Action Plan within the EU New Green Deal Strategy). Quantification of these impacts is not a simple task, as it requires understanding how and how much agricultural activities condition the many interrelated physical processes involved in the flow of water and transport of solutes in the complex soil–vegetation–atmosphere system at applicative (from field to irrigation district, to basin) scales.

To do that, scientists have been asked to provide tools to support decisions by land and water managers, to analyse impacts coming from alternative soil, water and crop management and for scenario analyses. To build these decision support tools, the already available models for simulating the fundamental soil water flow and solute transport processes have been frequently coupled to other existing models dealing with nutrient and soil organic matter management, crop growth, pesticides. For example, the well-known SWAP model [2], which provides a detailed description of the water flow and drainage processes even in fractured soils, has been frequently combined to the ANIMO model [3] to describe nutrients transport.

As already mentioned in the paper 1 [4], making these tools actually widespread requires the main agro-hydrological processes involved in the water, nutrients, organic matter transformations and transport be integrated in a single model, possibly with a user-friendly graphical interface allowing the model to be run even by researchers and water and agricultural office technicians with less academic experience. It also requires the ability to run such processes at multiple sites allowing for large-scale applications.

With these premises, this paper completes the paper 1 [4], describing the water flow and solute transport core of FLOWS, with a description of modules for specific applications in agro-hydrological modelling. Specifically, this paper will provide details on the FLOWS components dealing with irrigation water management, soil organic matter decomposition and CO_2 production, nitrogen and phosphorus transformations and transport. All these processes can also be run in the multisite configuration. Since many of these processes are mediated by the temperature, a short description of the Temperature module in FLOWS will also be given.

Therefore, the paper addresses first the irrigation management in FLOWS; it describes the theoretical framework for irrigation calculations and then it describes the graphical interface controlling irrigation management. Then, the paper addresses the temperature modelling in FLOWS, also along with the graphical interface controlling temperature simulations. Then, the paper describes the nutrient transformation and transport simulations in FLOWS, first by describing the organic matter decomposition, and the associated carbon, nitrogen and phosphorus transport, then by describing nitrogen transport only independently from the organic matter decomposition. The paper also summarizes the graphical interface regarding the organic and mineral fertilizer addition. Finally, although FLOWS has been used for several theoretical and applicative studies [5–10], this paper focuses on two large-scale applications of FLOWS related to irrigation and nutrient management.

2 FLOWS modules for specific applications in agro-hydrological modelling

2.1 Irrigation

In the case of irrigation, irrigation fluxes, q_{irr}, are added to the atmospheric (rainfall) fluxes, q_{surf}. The irrigation fluxes may come either from irrigation volumes actually supplied by a farmer or irrigation volumes calculated by the model according to a criterion based on the average pressure head in the root depth, D_r (see the section below on the irrigation criterion adopted by the code).

2.1.1 Irrigation options

FLOWS considers three options: (1) No irrigation; (2) Irrigation calculated by the model; (3) Irrigation provided by the user; and 4) Irrigation calculated the daily

evapotranspiration requirements. The latter allows for calculating daily irrigation fluxes equal to the potential evapotranspiration fluxes, ETp.

2.1.1.1 Irrigation calculated by the model With this option, the model optimizes irrigation fluxes. This optimization is achieved by maximizing root water uptake and minimizing deep percolation, while avoiding water stress. This strategy is followed in several numerical methods aimed at optimizing irrigation or regulating soil moisture in the root zone [11, 12].

The criterion used by the model to calculate the time for irrigation and the irrigation volume is based on a comparison between a pressure head, h_{av}, averaged over a user-given irrigation depth, z_{irr}, as simulated by the model, with a critical pressure head, h_{crit}, inducing some stresses to the crop (in terms of yield, product quality, …). Typically, z_{irr} should be set as D_{r}. Schematically, the irrigation criterion is summarized in Fig. 1a, b.

If h_{av} remains higher than the critical pressure head, h_{crit}, the average pressure head h lies above the stress condition, and no irrigation is required (Fig. 1a). Irrigation starts any time h_{av} becomes lower than h_{crit} (Fig. 1b). In other words, it is assumed that stress starts when the average pressure head, along the user-given z_{irr} (usually set as the rooting depth, D_{r}), becomes lower than the threshold for water stress.

Irrigation aims to bring the actual water content at each depth to the water content at field capacity. At the beginning of each simulation input time (t_{star} in the code), the model calculates the gross irrigation height as the difference of water storage, Δ_{stor}, between the water content at the field capacity and the actual water content in the *irrigation depth*, z_{irr}, to be supplied on that day. The *irrigation depth* is the depth over which the h_{av}, to be compared to h_{crit}, is computed by the model. The *irrigation depth* may be set at any value even if a reasonable value should be the maximum root depth, D_r;

$$\Delta_{stor} = \int_0^{z_{irr}} (\theta_{fc} - \theta(z))\, dz (cm of water) \tag{1}$$

Figure 2 provides a schematic view of this calculation.

Net irrigation, $q_{irr,net}$, to be supplied on day t is calculated as the difference between $q_{irr,gross}$ and the eventual rain falling at the time when the irrigation starts:

$$q_{irr,net} = q_{irr,gross} - q_{surf} \tag{2}$$

If the rainfall exceeds $q_{irr,gross}$, irrigation water is not supplied.

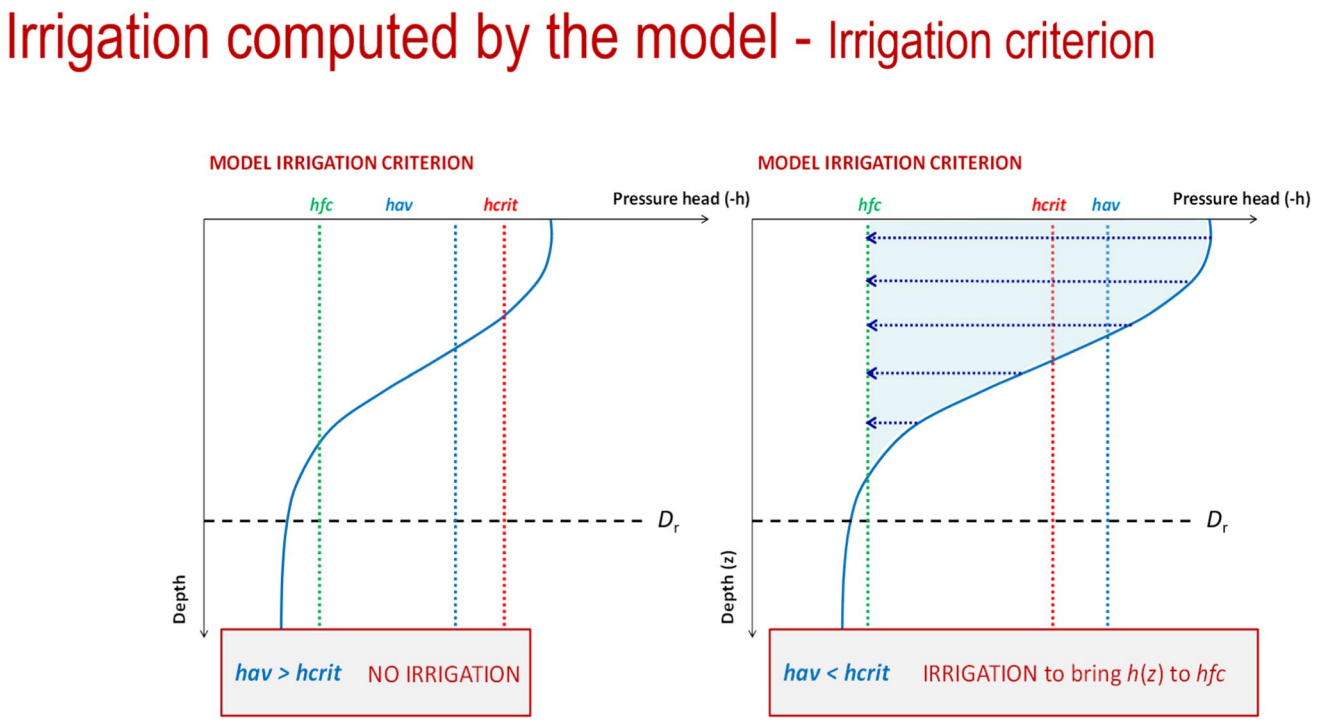


Fig. 1 Graphical view of the criterion used by the model to calculate the time for irrigation and the irrigation volume. **a** h_{av} higher than h_{crit}, no irrigation is required; **b** h_{av} lower than h_{crit}, irrigation is required to bring the pressure head at the field capacity, h_{fc}. Note that the blue curve is the actual distribution of the soil water pressure head along the soil profile, whose average is h_{av}

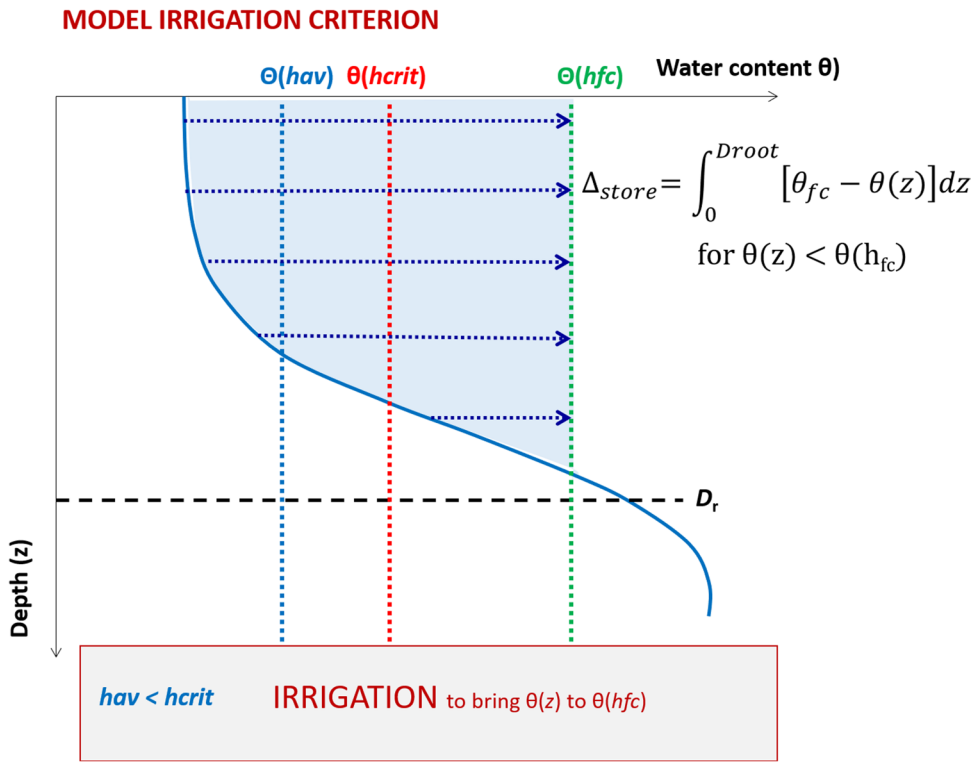


Fig. 2 Graphical view of the irrigation volume calculation according to the criterion shown in Fig. 1

It is also possible to select an on-farm irrigation efficiency, IE, of the irrigation system used for the crop considered, so that the actual irrigation amount, $q_{irr,act,}$ may be obtained as:

$$q_{irr,act} = q_{irr,net}/IE(cmofwater) \quad (3)$$

The code allows for selecting the periods of irrigation during the growth season, as well as the soil depth to be irrigated and the threshold value, h_{crit}, for irrigation.

2.1.1.2 Irrigation provided by the user With this option, the model allows the user to introduce the q_{irr} fluxes in addition to the fluxes coming from rainfall, q_{surf}.

2.1.1.3 Irrigation calculated the daily evapotranspiration requirements With this option, the model calculates the irrigation fluxes equal to the daily potential evapotranspiration, ET_p. The required inputs include the daily evolution of the reference evapotranspiration, ET_r, and the crop coefficient, K_c. The model then calculates ET_p as ($K_c \times ET_r$) and supplies the daily net irrigation fluxes equal to ET_p.

2.1.2 FLOWS graphical interface controlling irrigation options

In the case of irrigation computed by the model, the following window shows up (Fig. 3) in the interface.

Where the user is required to set the parameters:

- the uniformity coefficient, which is a numerical indicator of how evenly irrigation depths are distributed across the field, for example, sprinkler irrigation usually has a higher uniformity coefficient than surface irrigation methods;
- the *threshold pressure* (the critical pressure h_{crit}) below which the "model irrigates";
- the *irrigation depth*, that is the depth over which the h_{av}, to be compared to h_{crit}, is computed by the model. The *irrigation depth* may be set at any value even if a reasonable value should be the maximum root depth D_r;
- the *irrigation intervals*. Up to five periods may be selected, by shifting the *Number of irrigation intervals* bar and entering the initial and final time for each interval. This is to allow the user to account for specific irrigation habits of farmers, who, for example, are used to stress the crop in some of the growth stages to improve

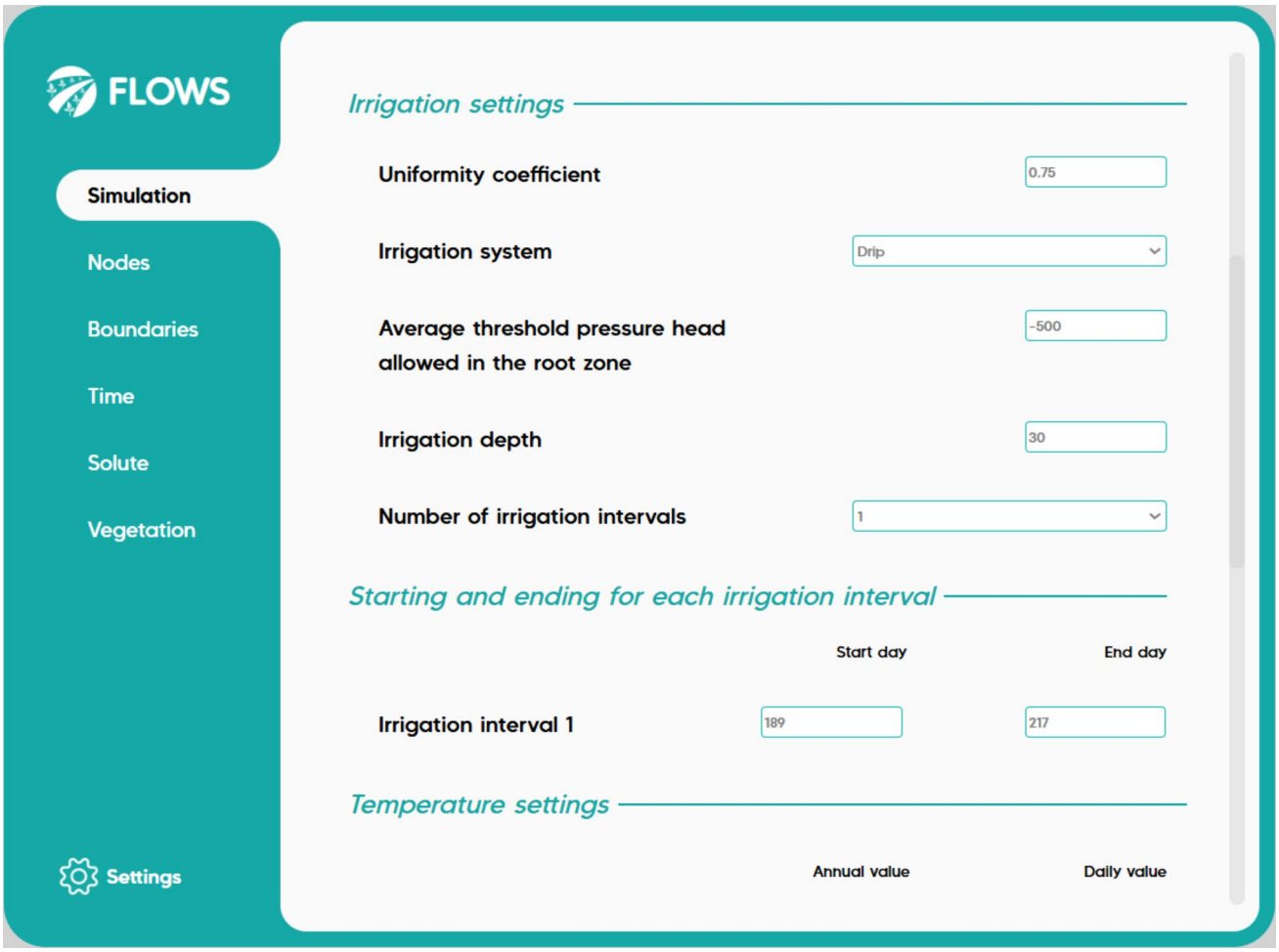


Fig. 3 Window for irrigation settings

organoleptic properties of the crop. By leaving the model "to irrigate" anytime $h_{av} < h_{crit}$, would not allow for taking into account the specific farmer behaviour.

In the case of irrigation provided by the user, the *time conditions* table will include a specific column to input the irrigation fluxes in cm/day.

2.2 Modelling temperature distribution in soil

Many physical, chemical, and biological processes in soils are influenced by soil temperature and its evolution in space and time. Thus, predicting and interpreting processes involving soil, water and vegetation interactions, also requires accurate modelling of the soil temperature distributions, $T(z, t)$, as a function of depth z and time t.

As explained later in Sect. 2.3, the soil temperature distribution is an important factor in the organic carbon, nitrogen and phosphorus module; temperature influences the fresh organic matter decomposition, and subsequently, the organic carbon, nitrogen and phosphorus mineralization, as well as the microbial and root respiration. Temperature distribution also affects the partitioning of CO_2 between gaseous and liquid phases. In addition, temperature affects the nitrification and denitrification rates.

In case of simulating nitrogen only (independently from organic matter decomposition), the temperature averaged over the fertilizer incorporation depth modifies rapid and slow organic-N mineralization, while the temperature at each node affects nitrogen immobilization.

Temperature modelling along a vertical soil profile is frequently carried out by considering the heat conduction equation [13]:

$$\frac{\partial T}{\partial t} = \frac{\partial}{\partial z} D_T \frac{\partial T}{\partial z} \tag{4}$$

where $D_T = \frac{\lambda_h}{C_h}$ is the soil thermal diffusivity (L^2T^{-1}), λ_h is the soil thermal conductivity and C_h is the soil volumetric heat capacity.

The equation above can be solved by assuming periodically variable heat fluxes at z = 0 and that at large depths, T becomes independent on the depth z. At z = 0, periodically variable heat fluxes results from both daily and annual cycles. At z = 0, the conductive heat flux, q_{cnd}, is:

$$q_{\mathrm{cnd}} = G = H - Rn - LE \tag{5}$$

where *H, Rn and LE* are respectively the convective heat flux, the net radiation and the evaporative (latent) heat flux. As for the bottom boundary condition, it is generally assumed that for $z \to \infty$ the temperature approaches the mean air temperature, T_a, so that $T(z,t)=T_a$.

Equation 4 assumes that the change in temperature over a given interval is governed only by heat conduction. Actually, as discussed by Holmes et al. [13], the convective heat flux, H is assumed to act in a very shallow surface layer, of 0.1–0.2 cm depth. As for the heat flux through evaporation, LE, it may extend to 5 cm below the surface for dry soils. So, to be rigorous, the right side of the equation should include a second term describing the latent energy loss, at least in the shallow boundary layer where evaporation takes place. Below this layer, the change in temperature is controlled only by heat conduction, as described by Eq. 4. In many numerical approaches to model soil temperature, this approximation is frequently extended to all depths below the soil surface and Eq. 4 is adopted to describe the temperature distribution along the whole soil profile. The solution to the heat flow equations proposed by van Wijk and De Vries [14] represents an early example of such an approximation. The authors described the daily and annual evolution of soil temperature by sine waves of amplitude A_T (°C), varying around an average temperature, T_{av} (°C). T_{av} is considered constant with depth, due to the assumption of heat conservation.

Assuming D_T to be constant with depth and time, a semi-infinite soil profile and the following sinusoidally varying temperature at the soil surface:

$$T(0,t) = T_{av} + A_T sin\left[1/2\pi + \omega\left(t - t_{Tmax}\right)\right] \tag{6}$$

van Wijk and De Vries [14] provided an analytical solution to Eq. 84 as:

$$T(z,t) = T_{av} + A_T e^{z/z_D} sin\left[1/2\pi + \omega\left(t - t_{Tmax}\right) - \frac{z}{z_D}\right] \tag{7}$$

with $\omega = 2\pi/\tau$ the angular frequency (1/d), τ the period of the wave (d), t the time starting from the January first and t_{Tmax} corresponding to the time when the temperature reaches the maximum. The damping depth, z_D, is the depth at which the amplitude of surface temperature oscillations is reduced by e^{-1} and is described as:

$$z_D = \sqrt{\frac{2D_T}{\omega}} \tag{8}$$

in general, the amplitude of the temperature wave is maximum at the soil surface and decreases with depth.

The solution above may be used for either diurnal ($\tau = 1$) or annual ($\tau = 365$) temperature evolution. For daily fluctuations, the maximum temperature occurs shortly after solar noon at the surface, but lags in time with increasing depth.

FLOWS model uses a combined approach, provided by van Wijk and De Vries [14], based on the superposition of the annual and daily sinusoidal fluctuation around a constant value of the soil. The approach sums two sinusoids, one for daily and the other for annual fluctuations, each having a constant amplitude and allows describing the daily fluctuations by accounting for the change of the daily average temperature at the surface over the year. Following this combined approach, the top boundary condition becomes:

$$\begin{aligned} &T(0,t) \\ &= T_{av,y} + A_{T,y}\sin\left[1/2\pi + \omega_y\left(t - t_{Tmax,y}\right) + A_{T,d}\sin\left[1/2\pi + \omega_d\left(t - t_{Tmax,d}\right)\right]\right] \end{aligned} \tag{9}$$

with subscripts y and d used respectively for annual and daily values.

In the equation, the term $T_{av,y} + A_{T,y} sin\left[1/2\pi + \omega_y\left(t - t_{Tmax,y}\right)\right]$ represents approximately the average temperature for the day corresponding to the time t, whereas the diurnal variation around this average temperature is described by the term $A_{T,d} sin\left[1/2\pi + \omega_d\left(t - t_{Tmax,d}\right)\right]$.

With the combined surface boundary condition, the temperature along the soil profile over time is obtained as:

$$\begin{aligned} T(z,t) &= T_{av,y} + A_{T,y} e^{-z/z_{D,y}} \sin\left[1/2\pi + \omega_y\left(t - t_{Tmax,y}\right) - \frac{z}{z_{D,y}}\right] \\ &+ A_{T,d} e^{-z/z_{D,d}} \sin\left[1/2\pi + \omega_d\left(t - t_{Tmax,d}\right) - \frac{z}{z_{D,d}}\right] \end{aligned} \tag{10}$$

The approach was also used by Elias et al. [15].

Assuming D_T (and thus the ratio $\frac{\lambda_h}{C_h}$) constant is an approximation of the real field soil conditions. Also, the boundary condition provided by Eq. 9 is not always a satisfying approximation for soil surface temperature. Finite difference numerical solutions of the Eq. 4 with λ_h and C_h not considered constant with depth and time provides more flexibility because may use more realistic boundary conditions [16–19].

However, when compared to experimental data, the analytical solution in Eq. 9 provides acceptable results [20].

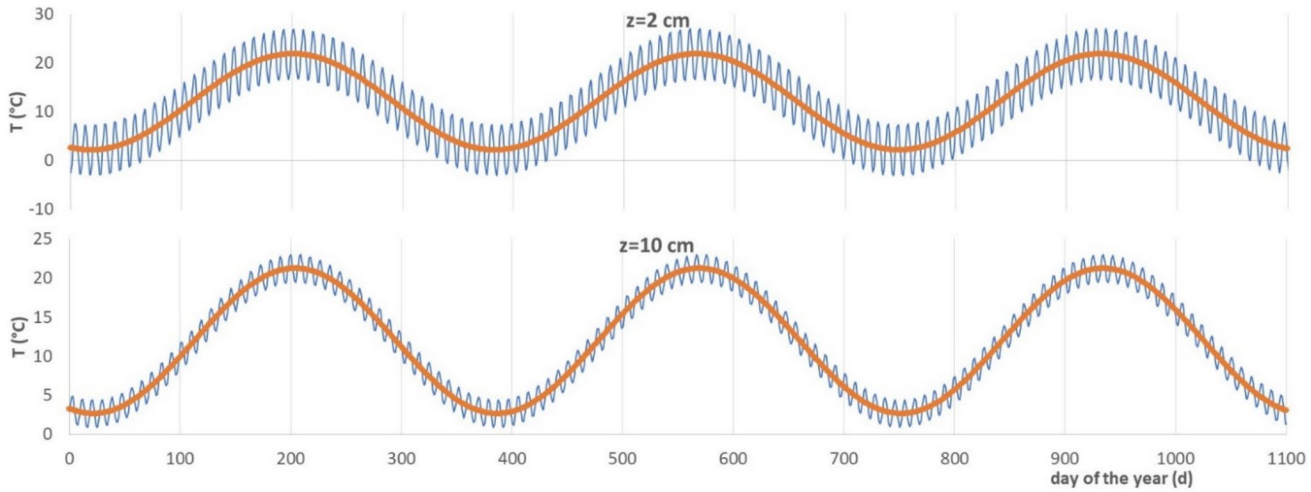


Fig. 4 Daily (blue lines) and yearly (orange lines) fluctuations of temperature at 2 cm and 10 cm depths over three years obtained using the parameters provided in the Table 1. The orange line and the blue line respectively provide the average daily temperature and the daily fluctuations about this average

Table 1 Temperature conditions at the soil surface and thermal diffusivity used for the graphs in Figs. 4 and 5

	T_{av} (°C)	A_T (°C)	ω (1/d)	τ (d)	t_{Tmax} (d)	D_T (cm^2/d)
Annual values (y)	12	10	0.0172	365	200	170
Daily values (d)		7	6.28	1	0.5	170

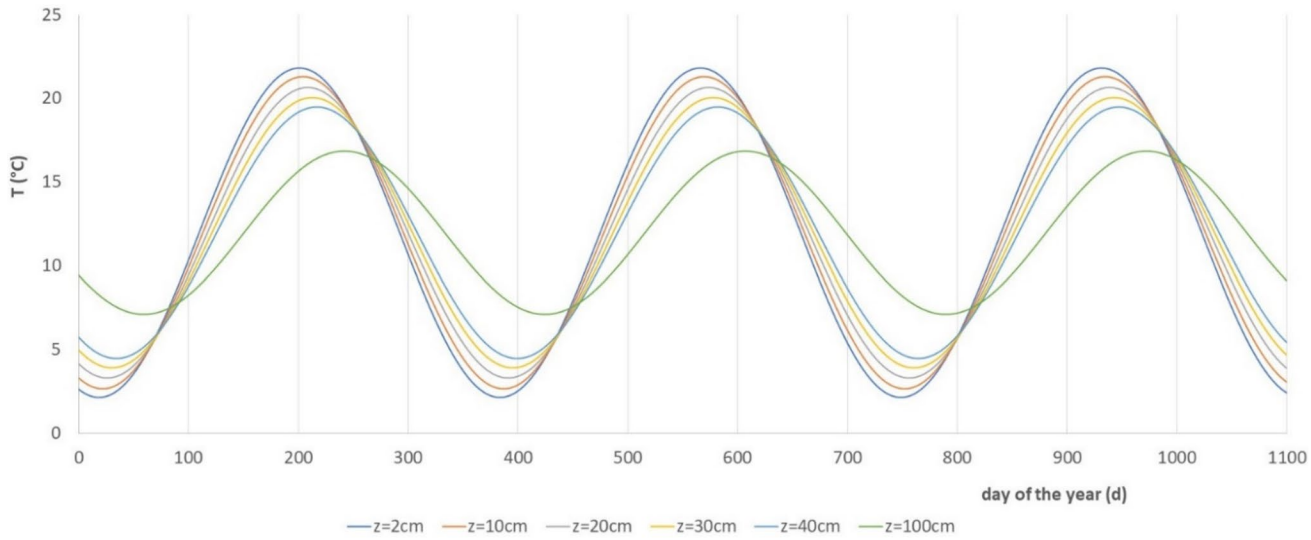


Fig. 5 Yearly fluctuations of average daily temperature at 6 depths over three years obtained using the parameters provided in the Table 1

More recently, Holmes et al. [13] evaluated the analytical solution to model soil temperature profiles in a bare soil. They found the commonly used solution to the heat flow equation by van Wijk and De Vries [14] perform well when applied at deeper soil layers. Higher errors were found when applying the model very close to the surface. These errors were found to be related to the overlooking of latent energy loss in the shallower soil layer below the surface, an issue which also remains for finite difference numerical solutions of the more general heat transport equation.

Figure 4 provides an example of application of Eq. 10 to a soil with the following temperature conditions and thermal diffusivity (Table 1).

Figure 5 provides the evolution of the average daily temperature over time at different depths for the same conditions given in the Table 1.

2.2.1 FLOWS graphical interface controlling temperature simulation

In the case of temperature profile computed by the model, the following window shows up (Fig. 6) in the interface.

Where the user is required to set the parameters:

- the *average annual temperature*, $T_{av,y}$ (°C);
- the daily and annual amplitudes, $A_{T,d}$ and $A_{T,y}$ (°C) of the sine wave oscillating around the average daily, $T_{av,y}$, and annual temperature;
- the daily, $t_{Tmax,d}$, and annual $t_{Tmax,y}$, time (days) when the temperature reaches the maximum.
- The diurnal, $\tau = 1$, and annual, $\tau = 365$, wave period;
- The soil thermal diffusivity, D_T, ($cm^2 day^{-1}$);
- The day of the year, t_{d0}, corresponding to the time t= 0 of the simulation.

These data can be obtained from site-specific observed hourly temperatures at the soil surface. If these field observations are unavailable, hourly air temperature data from a nearby agrometeorological station or a gridded land-reanalysis product may be used to obtain initial estimates, although calibration against local soil-temperature measurements is recommended because surface temperature is affected by vegetation, soil water content, residue cover and other surface conditions.

2.3 Nutrients transformations and transport in soil

FLOWS model handles additions of fertilizers as organic matter in the forms of manure and crop residue, as well as mineral fertilizers. The model requires the incorporation depth (called z_{fert} in the FLOWS code) as input. It is assumed that fertilizer addition is distributed uniformly along the incorporation depth. FLOWS allows for: (1) Simulating Organic Matter decomposition and Carbon, Nitrogen and Phosphorus transport. In this case, carbon, nitrogen and phosphorus transformations are all controlled by the dynamics of the organic matter decomposition and, thus, also by the C:N and C:P ratios; (2) Simulating only Nitrogen transport. In this second case, nitrogen mineralization is

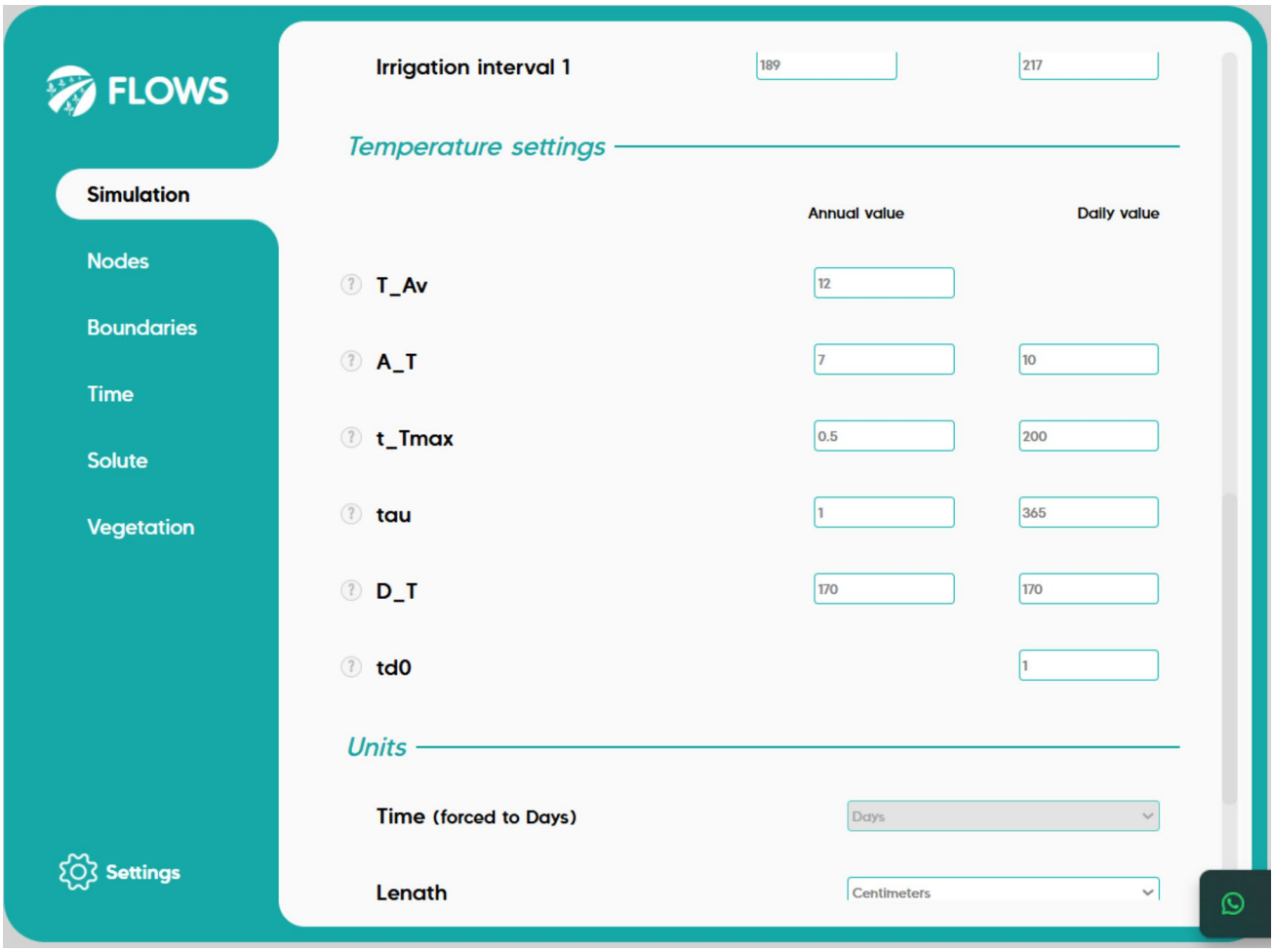


Fig. 6 Window for temperature settings

simulated as an empirical decay reaction and independently on organic matter decomposition dynamics, thus without accounting for the C:N ratio in the organic matter [21–23].

2.3.1 Simulating organic matter decomposition and carbon, nitrogen and phosphorus transport

FLOWS handles additions of nutrients in the forms of manure, crop residue, mineral fertilizers. The model also assumes that manure applications contain 50% of urea and 50% of organic matter [24].

2.3.1.1 Production of carbon, nitrogen and phosphorus from organic matter FLOWS considers two pools of organic matter: (1) Fresh Organic Matter (FOM) and (2) Stable Organic Matter or Humus (SOM) [25]. FOM consists of organic matter in manure and crop residue (RSD), plus microbial biomass (MCB). SOM comes from a relatively fast microbial-induced decay of FOM. SOM, in turn, also decays due to microbial activity. The decay of both SOM and FOM produces carbon dioxide (CO_2), N-NH_4 and P-PO_4, which are thus transported in soil in both gas (the CO_2) and liquid phases (CO_2, N-NH_4 and P-PO_4).

In the following, the fate of Carbon, Nitrogen and Phosphorus will be dealt with separately, even if, as obvious, they are strictly interrelated.

Organic carbon transformation processes in FLOWS

In FLOWS, the FOM decay is described as a first order decay chain according to the approach proposed by Jones et al. [26] (see Fig. 7) and used in the EPIC model [25].

The instantaneous rate of mineralization of FOM, rC_{fd} (g cm^{-2} d^{-1}) (from now on, the prefix *r* is for rate):

$$rC_{fd} = K_{fd} C_{FOM} exp\left(-K_{fd} t\right) \tag{11}$$

follows an exponential decay according to a decay parameter, K_{fd} (d^{-1}) obtained from an optimal decay constant for fresh organic matter, K_{fom}, which is reduced according to four reduction factors related to the soil temperature, F_T, water content, F_w, the carbon–nitrogen ratio and the carbon – phosphorus ratio, F_{CN} and F_{CP}, respectively:

$$K_{fd} = K_{fom} F_T F_w^{0.5} min\left(F_{CN} F_{CP}\right) \tag{12}$$

The four reduction factors calculations are reported in the following table (Table 2).

In Table 2, θ and θ_{fc} are the actual water content and the water content at field capacity, C_{FOM}, N_{FOM}, P_{FOM} (g cm^{-2}) are the carbon, nitrogen and phosphorus content of the FOM, N_{IN} and P_{IN} (g cm^{-2}) are the nitrogen and the phosphorus contents form inorganic sources (mineral fertilizers). All the organic matter transformations are assumed to involve the whole FOM in soil. Thus, all the reduction factors in Table 2 are calculated as averages in the whole incorporation depth, z_{fert}.

Following the approach proposed by Jones et al. [26], FLOWS assumes that about 20 percent of the carbon contained in the FOM, C_{FOM}, coming from the carbon in the microbial mass, C_{MCB}, and that in the residuals, C_{RSD}, mineralizes rapidly at a rate appropriate to non-structural carbohydrates. According to the same approach, about 70 percent of the residue mineralizes more slowly at a rate typical of cellulose-like materials, whereas the remaining 10 percent decomposes even more slowly at a rate appropriate to lignin. Accordingly, K_{fom}, assumes a different value depending on the ratio of the FOM to be still unmineralized, FOM_{unm}, to the initial FOM, FOM_{in}, in the fertilization depth, z_{fert} (see Eq. 13 in Table 2).

About 20 percent of the carbon coming from mineralization (0.2 rC_{fd}) is incorporated into the stable organic matter

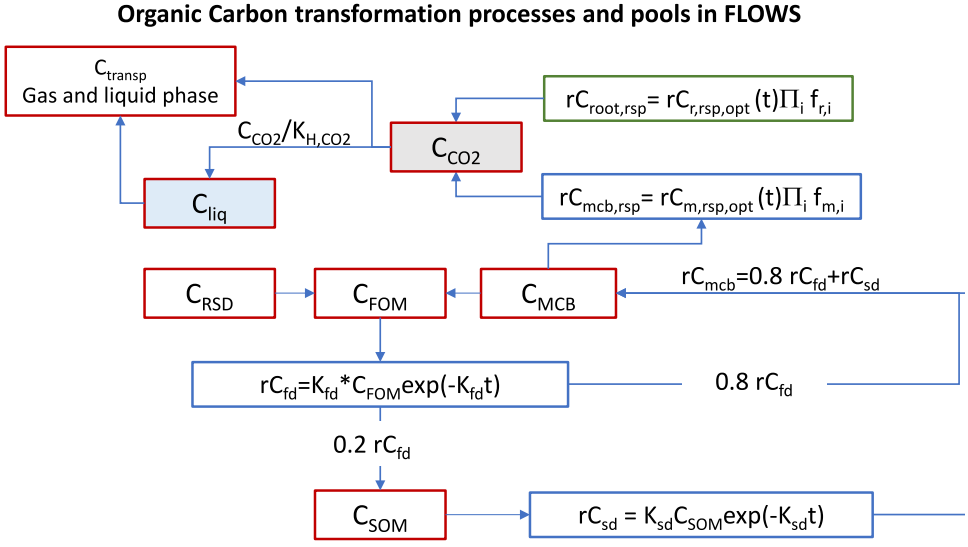


Fig. 7 Schematic view of organic carbon transformation processes and CO_2 production in FLOWS. Red blocks are pools, blue blocks are rates and the green block refers to the CO_2 root respiration rate. The prefix *r* is for rates. Labels meaning: *fd*= decay of FOM to stable and microbes pools; *SD*= decay of SOM to microbes pool; *mcb,rsp*=microbes respiration; *root,rsp*=root respiration; $C_{m,rsp,opt}$=optimal CO_2 production by microbial respiration; $C_{r,rsp,opt}$=optimal CO_2 production by root respiration; $K_{H,CO2}$=Henry's constant for CO_2; *R*=universal gas constant

Table 2 Reduction factors for the fresh organic matter decay constant, K_{fom} [26]

Decay constant, K_{fom}	$K_{fom} = 0.8\frac{FOM_{unm}}{FOM_{in}} \geq 0.8$ $K_{fom} = 0.050.8 > \frac{FOM_{unm}}{FOM_{in}} \geq 0.1$ $K_{fom} = 0.0095\frac{FOM_{unm}}{FOM_{in}} < 0.1$	(13)
Temperature reduction factor	$F_T = 0.9T/[T + \exp(7.63 - 0.312T)]$	(14)
Water content reduction factor	$F_w = \frac{\theta}{\theta_{fc}} \theta < \theta_{fc}$ $F_w = \frac{\theta_{fc}}{\theta} \theta \geq \theta_{fc}$	(15)
C:N reduction factor	$F_{CN} = \exp\left[-0.693\left(\frac{C_{FOM}}{N_{FOM} + N_{IN}} - 25\right)/25\right]$	(16)
C:P reduction factor	$F_{CP} = \exp\left[-0.693\left(\frac{C_{FOM}}{P_{FOM} + P_{IN}} - 200\right)/200\right]$	(17)

Table 3 Equations for calculation of the factors for the dependence of microbial (Eq. 19) and root (Eq. 20) respiration on soil depth (z), pressure head (h), temperature (T) and CO_2 concentration [27]

Depth dependence, *f(z)* (cm^{-1})	$f(z) = g(z)$		(21)
Water content (pressure head) dependence, *f(h)* (dimensionless)	$f(h) = \frac{log\lvert h\rvert - log\lvert h_1\rvert}{log\lvert h_2\rvert - log\lvert h_1\rvert}$ $f(h) = \frac{log\lvert h\rvert - log\lvert h_3\rvert}{log\lvert h_2\rvert - log\lvert h_3\rvert}$ $f(h) = 0$	$h_1 < h < h_2$ $h_2 < h < h_3$ $h < h_3; h > h_1$	(22)
Temperature dependence, *f(T)* (dimensionless)	$f(T) = \exp\left[\frac{E(T - T_{20})}{RTT_{20}}\right]$		(23)
CO2 dependence on its own concentration, *f(CO_2)* (dimensionless)	$f(CO2) = \frac{0.21C_{CO2,g}}{0.42 - C_{CO2,g} - K_M^*}$		(24)

(C_{SOM}) (the humus pool). The remaining (0.8 rC_{fd}) goes to the microbes' pool and will be partly respired (see below).

The carbon in C_{SOM}, in turn, will mineralize according to a first order rate constant, K_{sd}:

$$rC_{sd} = K_{sd}C_{FOM}exp(-K_{sd}t) \quad (18)$$

The carbon mineralized from the C_{SOM} will cumulate to that coming from the FOM and will follow the same fate. Partly, the total mineralized carbon will be used by the microbes (rC_{mcb}) and partly will go to CO_2 by microbial respiration at a rate $rC_{mcb,rsp}$.

Microbial and root respiration

FLOWS calculates microbial respiration, $rC_{mcb,rsp}$, and root respiration, $rC_{root,rsp}$ in a similar way, by following the approach proposed by Simunek and Suarez [27].

FLOWS considers only the production of CO_2 from microbial and root respiration, whereas neglects that coming from other chemical reactions with soil organic and mineral components, by assuming them of relatively minor importance for CO_2 balance in soil. According to Simunek and Suarez [27], optimal CO_2 production coming from microbial respiration, $rC_{m,rsp,opt}$ (g cm^{-2} d^{-1}), and root respiration, $rC_{r,rsp,opt}$ (g cm^{-2} d^{-1}), is assumed to be a function of soil depth and is affected by water content (or pressure head), temperature, pre-existing CO_2 concentration in soil. Both the diurnal and seasonal influences are assumed to be already accounted for by the effect of the temperature.

Thus, the microbial and root respiration (g cm^{-3} d^{-1}) are calculated by Eqs. 19 and 20, respectively:

$$rC_{mcb,rsp} = rC_{m,rsp,opt}f(z)f(h)f(T)f(CO_2) \quad (19)$$

$$rC_{root,rsp} = rC_{r,rsp,opt}f(z)f(h)f(T)f(CO_2) \quad (20)$$

The equations for calculating the factors in Eqs. 19–20 are summarised in Table 3.

With *g(z)* being the root distribution function (see the first companion paper), $C_{CO2,g}$ the concentration of CO_2 in the gas phase, $K_M^* = 0.21 - K_M$, with K_M the Michaelis–Menten constant, R the universal gas constant (8.314 J mol^{-1} K^{-1}), T the absolute temperature (°C + 273.15), T_{20}=293.15 K and E the activation energy for the reaction. According to Suarez and Simunek (1993), FLOWS assumes K_M^* =0.19 cm^3cm^{-3}, E=5000 J mol^{-1}, the pressure head for optimal soil respiration, $h_2 = -100$ cm in water column, the pressure head when

respiration ceases, $h_3 = -10^7$ cm and the pressure head when the soil is in close-to-saturation (anaerobiosis point), h_1 = air entry pressure head. Note that T_{20} is the temperature when f(T)=1. For T> T_{20} f(T)>1 and for T< T_{20} f(T)<1.

FLOWS uses a default value of 0.00036 g cm^{-2} d^{-1} for $rC_{r,rsp,opt}$, corresponding to the value of 0.002 m^3 m^{-2} d^{-1} suggested by Suarez and Simunek, 1993 and assuming carbon dioxide weight 0.001836 g cm^{-3} (at the pressure of 1 atm = 101,325 Pa and temperature of 25 °C). As for optimal microbial respiration, FLOWS assumes $rC_{m,rsp,opt}$ =0.4 rC_{fsm} + 0.6 rC_{sm}.

In fact, given an average Carbon Use Efficiency of 0.4 [26, 28], 0.4 of rC_{sm} and 0.32 of C_{fsm} (0.4 of 0.8 C_{fsm}) should be used to build the microbial biomass (immobilization), while the complement to 1 of rC_{sm} (0.6) and of rC_{fsm} (0.48) should be used for microbial respiration. In FLOWS, the immobilized C adds to the microbial pool (C_{MCB}) and thus to the fresh organic matter (C_{FOM}) pool.

The respiration from roots and microbes are assumed to be additive, so that the production rate of CO_2 coming from respiration (rC_{CO2}) (g cm^{-3} d^{-1}) is:

$$rC_{CO2} = rC_{mcb,rsp} + rC_{root,rsp} \tag{25}$$

rC_{CO2} will partly pass to liquid phase, C_{liq}, according to the following equation:

$$C_{liq} = \frac{rC_{CO2}}{K_{H,CO2}} \tag{26}$$

while the residual part, C_{gas}, will remain in gas phase. Both are passed to the ADE for transport process. Both C_{liq} and C_{gas} will be in g cm^{-2} d^{-1}. They are thus divided by the incorporation depth, z_{fert}, to obtain the concentrations in each calculation node in g cm^{-3} d^{-1} required by the ADE.

In Eq. 26, $K_{H,CO2}$ is the Henry's constant for CO_2 (dimensionless). It is obtained as [29].

$$K_{H,CO2} = \frac{1}{H_{cc}} = \frac{C_{gas}}{C_{liq}}$$

$$H_{cc} = H_{cp}RT$$

$$H_{cp} = \frac{C_{liq}}{p} \tag{27}$$

with H_{cp} the Henry solubility (mol m^{-3} Pa^{-1}), expressed as the ratio of the concentration of a species in the liquid (aqueous) phase and the partial pressure, p (Pa) of that species in the gas phase under equilibrium conditions. For the CO_2, H_{cp} is 0.00034 mol m^{-3} Pa^{-1} (see Table 6 in Sander [29]). H_{cc} is the dimensionless Henry solubility, R is the gas constant (8.314 J mol^{-1} K^{-1}) and T the absolute temperature (°C + 273.15).

Organic nitrogen and phosphorus transformation processes in FLOWS

Organic Nitrogen and Phosphorus are introduced in FLOWS by a fertilizers table. The organic nitrogen and phosphorus transformations considered in FLOWS are summarised schematically in Figs. 8 and 9.

In FLOWS, organic nitrogen and phosphorus mineralization follows the same path of the carbon and the immobilization rates (rN_{mcb} and rP_{mcb}) are proportional to that of the carbon according to C:N and the C:P ratios of the microbial mass in soil, which are assumed to be about 8.5 and 60, respectively [30, 31]:

Nitrogen immobilization (compare Figs. 7 and 8)

$$rN_{mcb} = \frac{rC_{mcb}}{CN_{ratio,mcb}} \tag{28}$$

Phosphorus immobilization (compare Figs. 7 and 9)

$$rP_{mcb} = \frac{rC_{mcb}}{CP_{ratio,mcb}} \tag{29}$$

In other words, N and P mineralize according to Eq. 11, with C_{FOM} replaced by N_{FOM} and P_{FOM}, respectively. Likewise, N_{SOM} and P_{SOM} decay according to Eq. 18. The nitrogen (N-NH_4 and N-NO_3) and phosphorus (P-PO_4) coming from organic mineralization enter into the mineral N-NH_4 and N-NO_3 and P-PO_4 pools and add to that eventually coming from mineral fertilizers, which for nitrogen can be urea ($UREA_{FRT}$), as well as solid and liquid NH_4 and NO_3 fertilizers (S&L_$NH4_{FERT}$, S&L_$NO3_{FERT}$) sources; for phosphorus, solid and liquid PO_4 fertilizers (S&L_$PO4_{FERT}$).

The subsequent fate of these different pools of mineral N-NH_4 and N-NO_3 and P-PO_4 is determined by different transformation reactions, frequently described as first-order decay, each with a specific constant, as well as by transport.

As for nitrogen, urea is hydrolysed according to a first-order decay with a constant k_{hyd}, producing NH_4. Part of this volatilizes according to a decay constant k_{vol}:

Urea hydrolysis and ammonium volatilization [32]

$$rNH4_{hUR} = UR_0 K_{hyd} \exp\left(-k_{hyd} t\right)$$

$$rNH3_{vUR} = NH4_{hUR} K_{vol} \exp\left(-k_{vol} t\right) \tag{30}$$

Beside immobilization, N-NH_4 and N-NO_3 in the soil solution (N-$NH4_{liq}$ and N-$NO3_{liq}$) phase may undergo nitrification (k_{nitr}) and denitrification (k_{den}), respectively. N-NH_4 may also be adsorbed to the solid fraction of the soil according to a linear isotherm with coefficient of distribution k_{ads}.

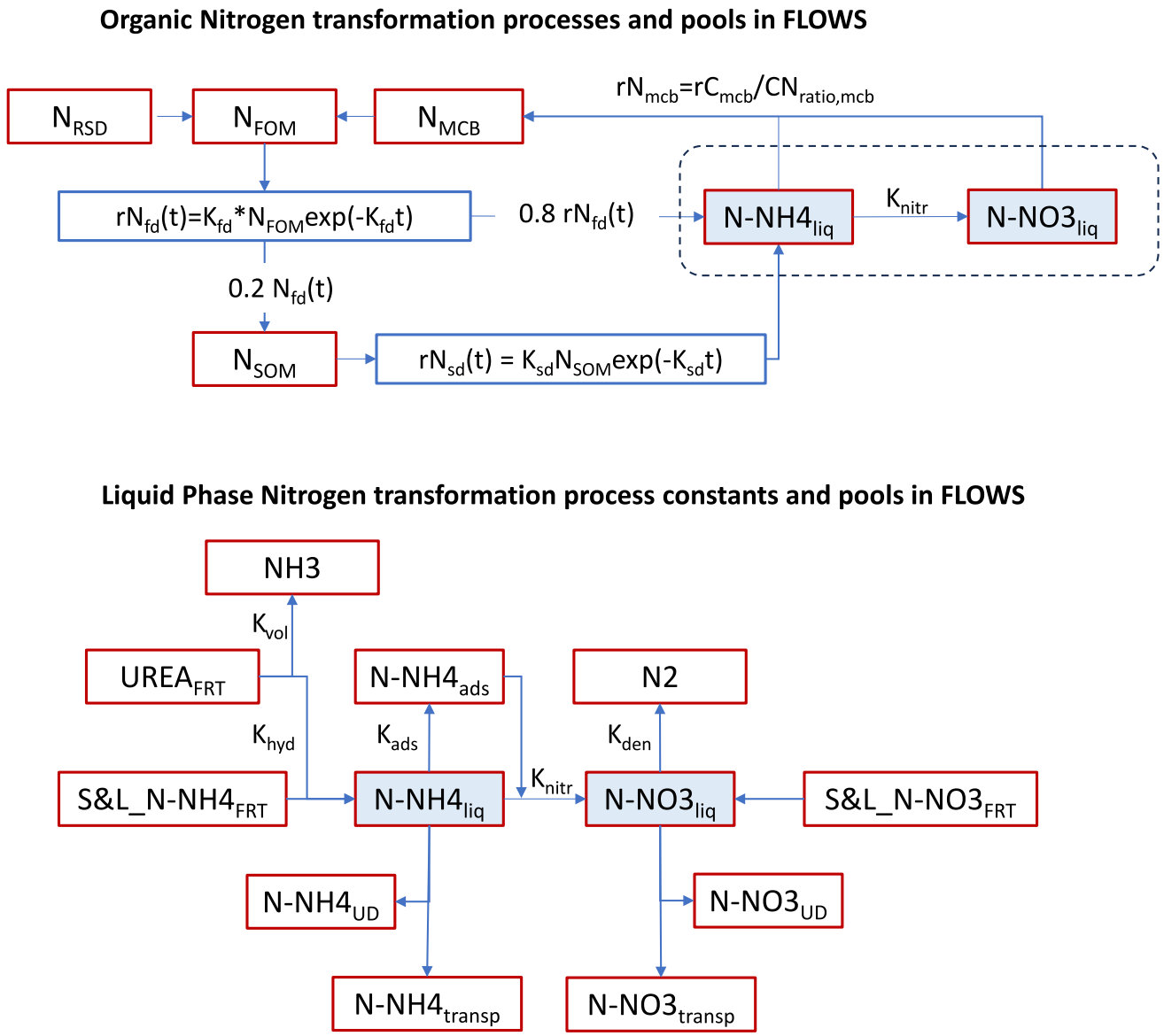


Fig. 8 Schematic view of organic and mineral nitrogen transformation processes in FLOWS. The mineralization follows the exact same paths already seen for organic carbon, with nitrogen mineralization proportional to that of the carbon. Constants K_{fd} and K_{sd} are the same as for carbon. The prefix *r* is for rates. The nitrogen immobilization in the microbial pool is regulated by the C:N ratio in the microbes ($CN_{ratio,mcb}$), which, according to Cleveland and Liptzin [30], is assumed to be 8.5. The meaning of pools and constants is given in the text

Finally, soil N-NH_4 and N-NO_3 may be drawn by root uptake and/or artificial drainage (both unified under a sink term, labelled by subscript UD).

The remaining N-NH_4 and N-NO_3 concentrations are thus transported through soil by advection–dispersion (subscript *transp* in Fig. 8). Accordingly, for nitrogen transport, the advection–dispersion equation (ADE) is used twice:

$$\frac{\partial \theta C_{NH}}{\partial t} + \rho_b \frac{\partial C_{a,NH}}{\partial t} = \frac{\partial q C_{NH}}{\partial z} + \frac{\left(\partial \theta D \frac{\partial C_{NH}}{\partial z}\right)}{\partial z} - Ss_{NH} \quad (31)$$

$$\frac{\partial \theta C_{NO}}{\partial t} + \rho_b \frac{\partial C_{a,NO}}{\partial t} = \frac{\partial q C_{NO}}{\partial z} + \frac{\left(\partial \theta D \frac{\partial C_{NO}}{\partial z}\right)}{\partial z} - Ss_{NO} \quad (32)$$

The subscripts NH and NO are for ammonium, N-NH_4, and nitrates, N-NO_3, forms of nitrogen, respectively. We assume here that both N-NH4 and N-NO3 may be adsorbed to the solid phase (the N-NO_3 on a positively charged surface). Note that the two equations are linked through the nitrification process which transforms part of the N-NH_4 (a sink for Eq. 31) to N-NO3 (a source for the Eq. 32).

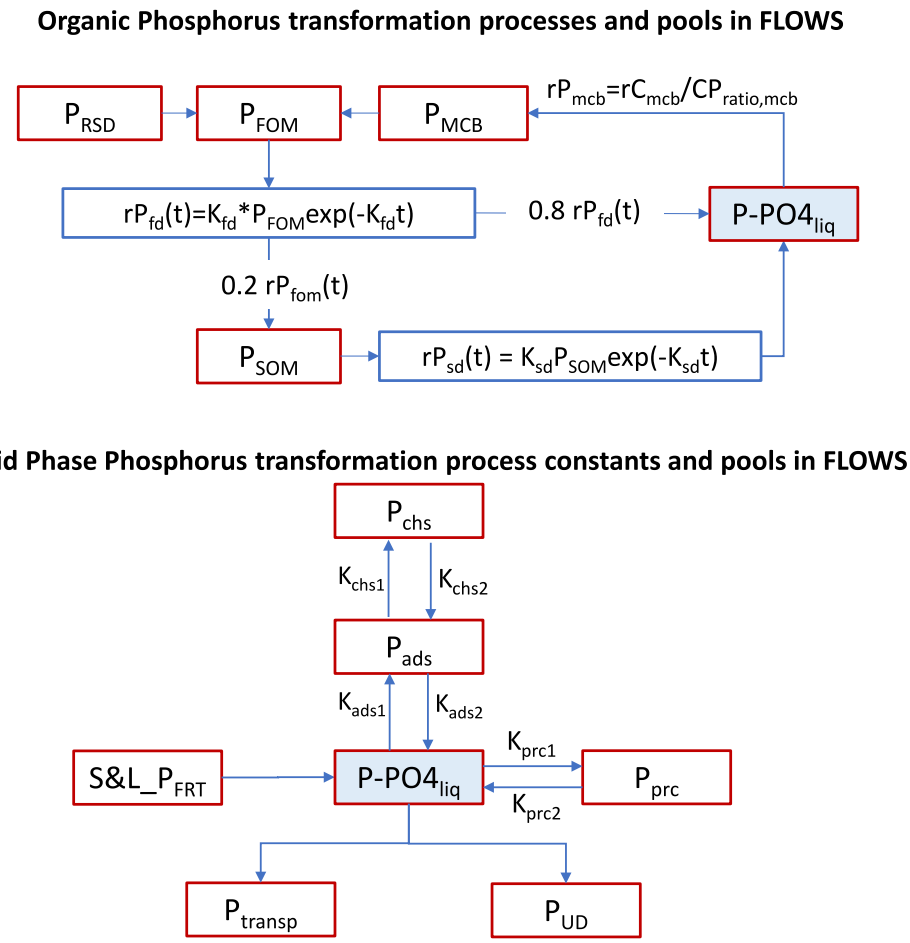


Fig. 9 Schematic view of organic and mineral phosphorus transformation processes in FLOWS. The mineralization follows the same paths already seen for organic carbon, with phosphorus mineralization proportional to that of the carbon. Constants K_{fd} and K_{sd} are the same as for carbon. The prefix *r* is for rates. The phosphorus immobilization in the microbial pool is regulated by the C:P ratio in the microbes ($CP_{ratio,mcb}$), which, according to Cleveland and Liptzin [30], is assumed to be 60. The meaning of pools and constants is given in the text

Table 4 The nitrogen transformation processes implemented in FLOWS. In the table, the *Ss* rates are in g/cm^3 of soil per day

Nitrification [33]	$Ss_{nit} = k_{nit} \times 1.07^{(T-T_{opt})} \frac{\theta}{\theta_{fc}} C_{NH} \theta \leq \theta_{fc}$	(34)
	$Ss_{nit} = k_{nit} \times 1.07^{(T-T_{opt})} \frac{\theta_{fc}}{\theta} C_{NH} \theta > \theta_{fc}$	
Denitrification [34, 35]	$Ss_{den} = 0 \theta \leq \theta_d$	(35)
	$Ss_{den} = k_{den} \times 1.07^{(T-T_{opt})} \frac{\theta - \theta_d}{\theta_{fc} - \theta} C_{NO} \theta_d \leq \theta \leq \theta_s$	
	$\theta_d = 0.627 \theta_{fc} - 0.0267 \frac{\theta_s - \theta}{\theta_s} \theta_{fc}$	
Root uptake of Nitrogen	$S_{upNH} = K_{r,NH} S_r C_{NH}$	(36)
	$S_{upNO} = K_{r,NO} S_r C_{NO}$	
Nitrogen losses to artificial drainage	$S_{drNH} = S_{dr} C_{NH}$	(37)
	$S_{drNO} = S_{dr} C_{NO}$	

Specifically, Ss_{NH} and Ss_{NO} in the Eqs. 31 and 32 are the source-sink terms of solute, all function of depth *z* and time *t*, and can be written respectively as:

$$Ss_{NH} = -Ss_{minNH} - Ss_{urea} - Ss_{frtNH} + Ss_{nit} + Ss_{vol} + Ss_{upNH} + Ss_{drNH}$$

$$Ss_{NO} = -Ss_{nit} - Ss_{frtNO} + Ss_{den} + Ss_{upNO} + Ss_{drNO} \quad (33)$$

where Ss_{minNH} and Ss_{urea} are the N-NH_4 coming from mineralization (see Eq. 11) and urea hydrolysis (see Eq. 30), respectively, Ss_{nit} is the N-NH4 transformed by nitrification, Ss_{imm} is the immobilized N-NO_3. Ss_{den} and Ss_{vol} are the N-NO3 and the N-NH4 lost by denitrification and volatilization, respectively. Ss_{upNH} and Ss_{upNO} are the N-NH4 and N-NO3 root uptake, respectively. Likewise, Ss_{drNH} and Ss_{drNO} refer to the N-NH4 and N-NO3 losses through the artificial drainage.

Finally, Ss_{frtNH} and Ss_{frtNO} are the N-NH_4 and N-NO_3 source terms coming from mineral fertilizers additions (other than urea).

The source terms Ss_{minNH}, Ss_{urea} Ss_{frtNH}, and Ss_{frtNO}, are obtained by dividing the mineralization, urea hydrolysis and mineral fertilizer addition rates (all in g/cm^2 of soil per day) by the incorporation depth, *zfert* (cm), to obtain the corresponding *Ss* terms (in g/cm^3 of soil per day) to be added to each of the calculation nodes within *zfert*.

Table 4 summarises the equations controlling the liquid phase nitrogen transformation processes considered in FLOWS and also schematically illustrated in the Fig. 8 in the block about *Liquid phase nitrogen transformation process constants and pools in FLOWS*.

In the Table 4, UR_0 and *UR_NH4* are the initial urea concentration and the N-NH_4 produced by the urea hydrolysis, respectively; k_{hUR} and k_{vUR} are the first-order rate coefficients for the two decay reactions (hydrolysis and volatilization, respectively).

k_{nit}, *and* k_{den}, are respectively the optimal first-order rate coefficients for nitrification of N-NH4, and denitrification of N-NO3; T is the actual soil temperature (°C); T_{opt} is the optimum temperature for the process (°C) [33]; θ_d is the threshold water content for denitrification.

$K_{r,NH}$ and $K_{r,NO}$ are the root uptake preference factors (dimensionless) for either the N-NH4 or the N-NO3, accounting for positive or negative selection of solute ions relative to the amount of soil water that is extracted [36]. For passive uptake, K_r=1.

S_r and S_{dr} are the source-sink terms related respectively to root uptake and artificial drainage respectively, and θ_{fc} is the water content at field capacity (assumed as the water content at pressure head h=−330 cm in water column).

As for phosphorus, FLOWS describes the fate of liquid phase phosphorus (P_{liq}) according to the decay reaction chains proposed by Mansell et al. [37]. In general, inorganic *P* is rapidly converted from orthophosphate to less soluble forms. Phosphorus soil solution concentrations generally observed after inorganic P supply to the soil are of the order of 1 µg/cm or less [38].

The initial rapid removal of phosphorus from the soil solution may be attributed to relatively fast reactions, such as physical adsorption to soil colloidal material. The adsorption of P is usually considered to be reversible [39, 40]. Other additional much slower reactions involve precipitation of phosphorus as AI, Fe, and Ca phosphates. Also, a portion of the physically adsorbed phosphorus may slowly become surrounded by matrices of Fe and AI components and become occluded (chemisorption). Mechanisms of adsorption, precipitation, and chemical immobilization operate simultaneously and continuously with time to remove phosphorus from the soil solution.

The Mansell et al. [37] approach, also adopted in FLOWS, assumes the transfer of phosphorus between solution, adsorbed, chemisorbed and precipitated to be controlled by six reversible reactions (see the block in the Fig. 9 about *Liquid phase phosphorus transformation process constants and pools in FLOWS*). While adsorption occurs on pore walls and colloids, chemisorption (also defined as occlusion by the Mansell et al. [37]) refers to (slow) transformation of weaker physical bonds of the adsorbed phosphorus to stronger chemical bonds. FLOWS assumes adsorption to follow a Nth order kinetic (with an average N of 0.35, as suggested by Mansell et al. [37]) and a constant K_{ads1}, whereas all the other reactions (desorption, chemisorption and mobilization, precipitation and dissolution) follow a first order kinetic, respectively with constants K_{ads2}, K_{chs1}, K_{chs2}, K_{prc1}, K_{prc2}, even if higher order may easily be developed in the code. Reactions rates depend on pH, nature and content of clay minerals, organic matter, carbonates, cation saturation and amount of phosphate applied. Table 5 summarises the equations controlling the liquid phase phosphorus transformation processes considered in FLOWS.

The remaining P-PO_4 concentrations are thus transported through soil by advection–dispersion (subscript *transp* in Fig. 9):

$$\frac{\partial \theta C_P}{\partial t} = \frac{\partial q C_P}{\partial z} + \frac{\left(\partial \theta D \frac{\partial C_P}{\partial z}\right)}{\partial z} - Ss_P \tag{38}$$

Table 5 The phosphorus transformation processes implemented in FLOWS [37]

Phosphorus adsorption	$Ss_{ads} = \frac{\partial\left(\rho_b C_{a,P}\right)}{\partial t} = K_{ads1}\theta C_P^N - \left(K_{ads2} + K_{chs1}\right)\rho_b C_{a,P} + K_{chs2} C_P$	(40)
Phosphorus chemisorption	$Ss_{chs} = \frac{\partial\left(\rho_b C_{c,P}\right)}{\partial t} = K_{chs1}\rho_b C_{a,P} - K_{chs2}\rho_b C_{c,P}$	(41)
Phosphorus precipitation	$Ss_{prc} = \frac{\partial\left(\rho_b C_{p,P}\right)}{\partial t} = K_{prc1}\theta C_P - K_{prc2}\rho_b C_{p,P}$	(42)
Root uptake of Phosphorus	$S_{upP} = K_{r,P} S_r C_P$	(43)
Phosphorus losses to artificial drainage	$Ss_{drP} = S_{dr} C_P$	(44)

In the table, the *Ss* reaction rates are in g/cm^3 of soil per day

with Ss_P being the sum of mineralized, adsorption, desorption, precipitation, dissolution, root uptake, drainage losses and fertilizer (organic/inorganic) components:

$$Ss_P = -Ss_{minP} - Ss_{frtP} - \theta\left(K_{ads1}C_P^N + K_{prc1}C_P\right) + \rho_b\left(K_{ads2}C_{a,P} + K_{prc2}C_{p,P}\right) + Ss_{upP} + Ss_{drP} \quad (39)$$

In Eq. 39, as well as in the equations in Table 5, subscript P is for P-PO4, whereas subscripts a, p and c are respectively for adsorbed, precipitated and chemisorbed phosphorus concentrations.

As for nitrogen, the source terms Ss_{minP} and Ss_{frtP}, are obtained by dividing the mineralization rate and mineral phosphorus fertilizer addition rates (all in g/cm^2 of soil per day) by the incorporation depth, *zfert* (cm), to obtain the corresponding *Ss* terms (in g/cm^3 of soil per day) to be added to each of the calculation nodes within *zfert*.

2.3.2 Simulating only nitrogen transport

FLOWS allows to simulate only nitrogen transport by partly following the empirical approach adopted in the RISK-N model [24] for the mineralization of organic nitrogen. In this case, soil organic N is conceptually divided into active and passive fractions [24]. The active fraction includes organic N involved in the process of mineralization and is divided into rapid and slow mineralization fractions. The rapidly mineralizing N consists of recent additions of manure and crop residue. The slow fraction consists of resident soil N still mineralizing, as well as the remaining organic N from past manure and crop residue applications.

As for the previous case, the model handles additions of nitrogen in the forms of manure, crop residue, mineral fertilizers. The model requires the incorporation depth (called *zfert* in the FLOWS code) as input. It is assumed that nitrogen addition is distributed uniformly along the incorporation depth. The model assume that manure applications contain 50% of urea and 50% of organic N. As for crop residues incorporation, it is assumed that 50% consists of rapidly mineralizing fraction, 45% of slowly mineralizing organic N and 5% is considered as passive fraction (Gusman and Marino, 1999).

Again, the mineralization process is assumed to be described by a first-order decay equation [21, 22]:

$$rNH4_{min} = k_{mOM}NOM_0\exp\left(-k_{mOM}t\right) \quad (45)$$

with $rNH4_{min}$ the rate of N-NH4 production from mineralization (g/cm^2 of soil per day), NOM_0 the initial pool of nitrogen in organic matter and k_{mOM} is a first order rate constant for the mineralization process. Now, the latter does not depend on the C/N ratio but still depends on soil temperature and water content, being a function of microbial processes. Also, as the mineralization rates change according to the type of organic N pools to be mineralized (rapid or slow), two different equations can be used to determine k_{mOM} in Eq. 45 [23]:

$$k_{mOM}(T) = k_{rp}(T) = 5.6\times10^{12}\exp\left(\frac{-9800}{T+273}\right)F_w$$

$$k_{mOM}(T) = k_{sw}(T) = 4.0\times10^{9}\exp\left(\frac{-8400}{T+273}\right)F_w \quad (46)$$

where T is the actual soil temperature (°C) and the water content factor for mineralization, F_w, is calculated as in Eq. 15. For the calculation of $k_{rp}(T)$ and $k_{sw}(T)$, FLOWS uses the averages of both F_w and T within the incorporation depth, *zfert*.

Again, $rNH4_{min}$ is divided by *zfert* to obtain the Ss_{frtNH}.

As for immobilization, in this case FLOWS does not consider the C/N ratio but follows an empirical equation decay [33]:

$$Ss_{imm} = k_{im}\times1.05^{(T-T_{opt})}F_wC_{NO}\theta \le \theta_{fc}$$

$$Ss_{imm} = k_{im}\times1.05^{(T-T_{opt})}\frac{1}{F_w}C_{NO}\theta > \theta_{fc} \quad (47)$$

with a decay constant k_{im} and where T_{opt} is the optimal temperature for the process. All the other processes (Urea hydrolysis; Ammonia volatilization (N-NH_4 to N-NH_3), Nitrification (N-NH_4 to N-NO_3); Denitrification (N-NO_3 to N-N^2); Plant uptake; Drainage losses, are all described by using the equations already seen for the previous case.

Again, the transport of N-NH_4 and N-NO_3 is described by solving simultaneously the Eqs. 31–32, with Ss_{NO} term in Eq. 33 now including also the Ss_{imm} losses.

In the case of nutrient transport FLOWS allows setting all the input parameter involved (see Fig. 10). Those parameters include: 1) the incorporation depth of fertilizers, *zfert* over which it is assumed that nitrogen addition is distributed uniformly; 2) the optimum temperature for the immobilization process, T_{opt}; 3) the first-order rate coefficient for the urea hydrolysis decay reaction, K_{hyd}; 4) the first-order rate coefficient for the urea volatilization decay reaction, K_{vol}; 5) the isotherm parameters (i.e., the slopes and exponents) of N-NO_3, N-NH_4 and P-PO_4 (in the case of simulating P-PO_4, the slope corresponds to the parameter K_{ads1} in the Fig. 9); 6) the root uptake factors for N-NO_3, N-NH_4 and P-PO_4; and the first order kinetic constants for phosphorus desorption, K_{ads2}, chemisorption, K_{chs1}, mobilization, K_{chs2}, precipitation, K_{prc1}, and dissolution, K_{prc2}. More information on the nutrient processes' simulations and interface can be found in Sects. 4.3 and A.2.5 in FLOWS handbook [41].

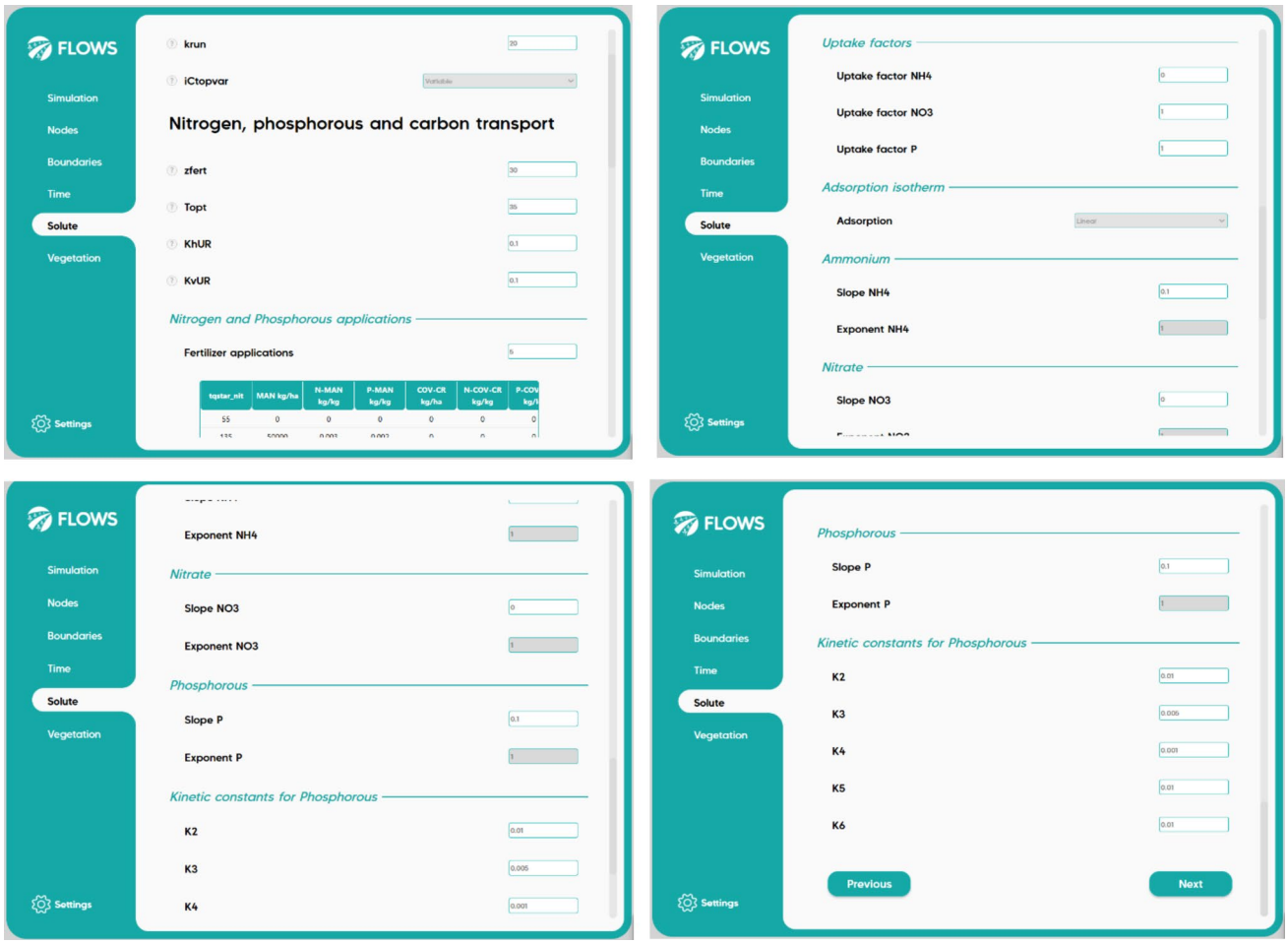


Fig. 10 The Nitrogen, Phosphorus and Carbon transport settings sub-block



Fig. 11 From Hassan et al. [10], the irrigation sector 6 in the Apulia region, Italy. The blue circles are the surface HP characterization points. The red circles are the five excavated soil profiles. The polygons bordered by black solid lines represent the 90 Thiessen polygons with unique surface HP. The polygons with red dashed lines represent the soil units

3 Some selected applications of the model

3.1 Using FLOWS for irrigation optimization at large scale

[10] used FLOWS to analyze the role of the spatial variability of soil Hydraulic Properties, HP, and Vegetation Properties, VP, on modelling agrohydrological processes with the aim of optimizing irrigation volumes at large scales. For this purpose, the study analyzed a 140-ha irrigation sector (sector 6), one of the 19 sectors constituting district 10 of the "Sinistra Ofanto" irrigated system in Foggia Province, Apulia Region, Southeast Italy (Fig. 11).

Ninety locations were selected to characterize the soil surface hydraulic properties using the tension infiltrometer method (the blue circles in Fig. 11). Five pits were excavated to obtain the HP and depths of different soil horizons (the red circles in Fig. 11). The irrigation sector was then divided into two sets of Thiessen polygons: five polygons representing the soil units (bordered by red dashed lines in Fig. 11) and 90 polygons representing the surface HP measurement

points (bordered by solid black lines in Fig. 11). Each of the 90 polygons was then assigned its own HP and VP.

In this context, FLOWS was used for optimizing the irrigation fluxes while accounting for the spatial variability of HP and VP. Parallelly, FLOWS also allowed for studying the uncertainty resulting from overlooking the spatial variability of HP and VP in order to find the minimum dataset of each to optimize irrigation fluxes at sector scale.

Preliminarily, FLOWS simulations were first carried out using the registered irrigation fluxes applied by the farmers in the study area to find the irrigation depth, z_{irr}, for specific crop and soil under a specific farmer behaviour, to be used as input in the model, along with the pressure head within z_{irr} induced by farmers' behaviour, by analysing the average simulated pressure head along the root zone and along the first soil horizon depth. Figure 12 shows the registered irrigation (light blue lines) and the precipitation (dark blue lines) fluxes, along with the simulated average pressure head in the root zone, of about 100 cm, (solid orange line) and in the first soil horizon depth, of about 45 cm, (dashed orange line) in a representative plot in sector 6 cultivated with wine grape.

Figure 12 illustrates the water pressure head developing under actual farmer behavior. From the graph, it can be

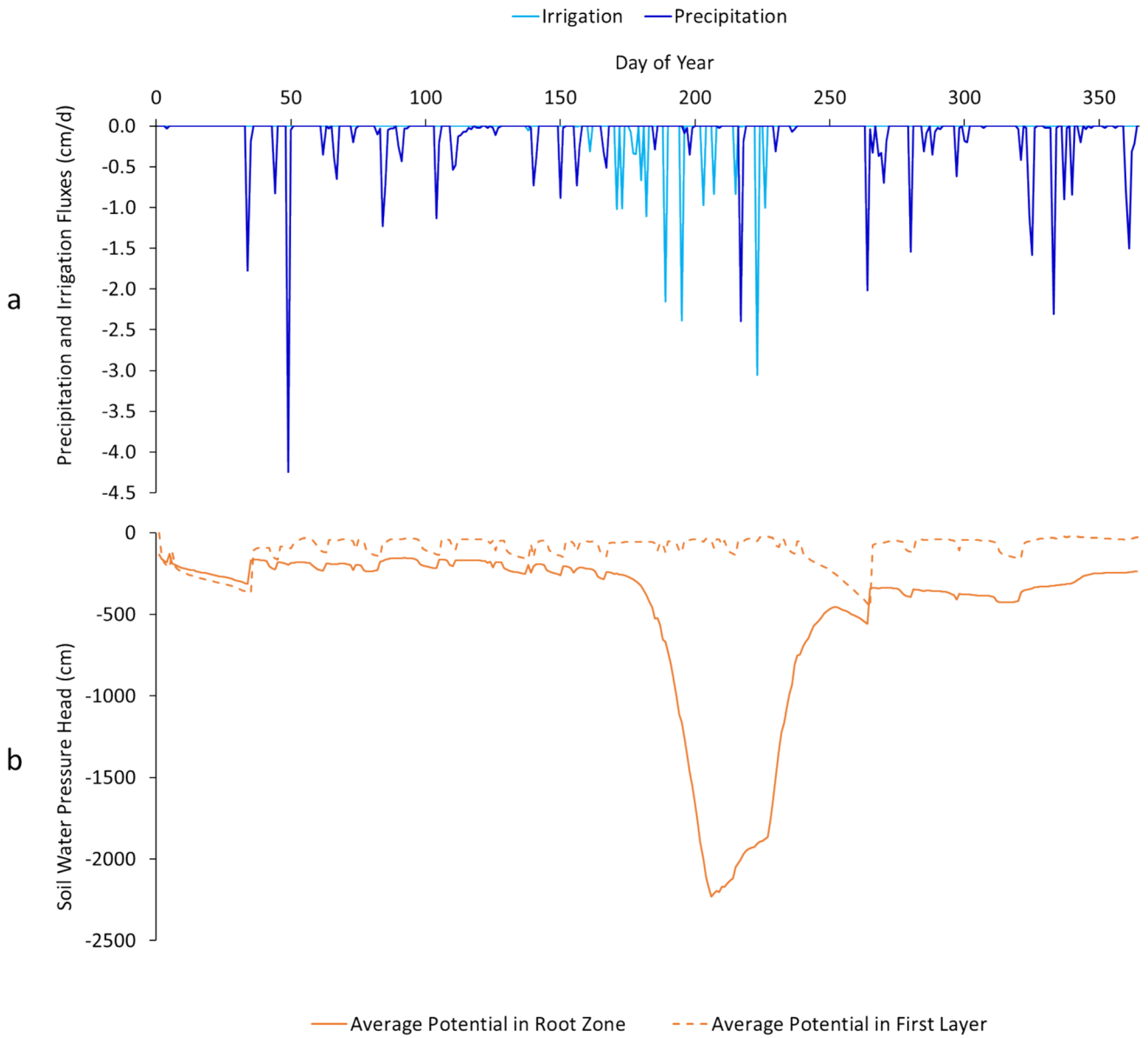


Fig. 12 **a** The daily irrigation and precipitation fluxes (light blue and dark blue lines, respectively), **b** the corresponding average soil water pressure head in the root zone (solid orange line) and in the first soil horizon depth (dashed orange line) in a representative plot cultivated with wine grape in the irrigation sector 6 of district 10 of the "Sinistra Ofanto" irrigated system. The critical water potential for the wine grape is $h_{crit} = -500$ cm. The root zone is of about 100 cm

observed that, through irrigation, the farmer tends to maintain the water pressure head above − 500 cm only in the first soil layer while allowing the pressure head throughout the root zone, of about 100 cm, to decrease well below h_{crit}. This may be justified by considering that the farmer deliberately seeks to induce a certain level of water stress to obtain specific organoleptic characteristics. Such behavior cannot be ignored when aiming for realistic, model-based irrigation management and should therefore be taken into account when optimizing irrigation fluxes by a model. This type of analyses may only be carried out by Richards equation-based models, such as FLOWS. Compared to capacity-based crop models, which are frequently based on so-called bucket approaches for describing the soil hydrological behavior, FLOWS, as all the models based on the solution of the Richards equation, predicts the evolution of the water pressure head distribution in the soil profile, which is known to be the actual (and physical) driving force for water fluxes along the soil profile [42].

Based on this analysis, Hassan et al. (2024) identified the z_{irr} required by FLOWS withing which the pressure head has to be kept within the −500 cm critical pressure head. Thus, another set of simulations was carried out by optimising irrigation fluxes. In this optimization scenario, the variability of HP and VP among the 90 Thiessen polygons was preserved; this scenario was thus referred to as the Detailed Variability Scenario (DVS). The DVS consisted of 90 simulations representing the 90 polygons, each including its corresponding HP and VP inputs. Following the DVS, a Reduced Variability Scenario, RVS, was studied. In the RVS case, simulations were simplified by using sparser data and fewer polygons to reduce the number of runs while maintaining sector-scale estimates of irrigation fluxes comparable to those from the DVS scenario.

First, VP variability was overlooked by assuming a fictitious crop with Uniform Vegetation Properties (UVP) across the sector, computed as area-weighted averages of crop parameters. This RVS-UVP setup still consisted of 90 simulations using 90 soil HP inputs and allowed assessment of the impact of using averaged vegetation instead of the actual cropping pattern.

Figure 13 shows the annual irrigation volumes in m^3/ha as applied by the farmers (a), optimized by FLOWS for the DVS (b) and as optimized by FLOWS for the RVS-UVP (c), for each of the 90 Thiessen polygons.

As shown in the figure, the optimized volumes in DVS, i.e., accounting for the observed variability of VP and HP, were less than the registered volumes applied by the farmers in most of the polygons. The overall average optimized volume for the DVS at sector scale was 1360 m^3/ha, compared to 1693 m^3/ha registered average volume at the same scale. The figure also shows how overlooking the VP variability did not significantly affect the simulation results. In fact, the overall average irrigation volumes at sector scale for the RVS-UVP was 1329 m^3/ha.

By using FLOWS in a multi-site configuration, FLOWS also allowed to carry out an uncertainty analysis was carried out by progressively reducing the number of soil HP inputs, N_s, (i.e., $N_s = 40, 35, 30, \ldots, 5$). For each case, controlled random combinations of soil profiles were selected by ensuring that these generated profiles were evenly distributed over the soil units (the red polygons in Fig. 11). Thiessen polygons were defined for each of the random combination of N_s profiles and the areas of those polygons were calculated. Then, the irrigation volumes were optimized for each of the N_s Thiessen polygons, and thus, sector-scale irrigation volumes were computed as area-weighted averages. Uncertainty associated with each N_s was calculated as the standard deviation of the computed irrigation volumes for the randomly generated combinations of N_s profiles.

Sector-scale average irrigation volumes were considered acceptable if it lied between 0.85 and 1.15 the average sector-scale irrigation computed for the DVS. The uncertainty associated with each N_s was considered acceptable if it was less than or equal to 1.25 of the uncertainty associated with $N_s = 40$. As a final step, five separate simulations were performed by representing the entire sector with a single soil profile, using the HP measured at each of the five excavated pits (the red circles in Fig. 11). This configuration, referred to as RVS-UHP, involved simulations with a unique HP input applied uniformly across the sector.

The uncertainty analysis led to three distinct behaviors as N_s decreases, based on average predictions and Inter-Quartile Range, IQR (see Fig. 14). Using 4–8 HP inputs per soil unit yielded reliable average irrigation estimates with low uncertainty (the plots in the blue rectangle in Fig. 14), closely matching the DVS configuration and confirming that more than 8 HP inputs per soil unit would be redundant and impractical. Using 1–3 HP inputs per soil unit still provided acceptable average and median predictions but with higher uncertainty due to limited representation of HP variability (the plots in the red rectangle in Fig. 14); notably, one profile per soil unit performs similarly to 3, though with more asymmetrical distributions. In contrast, using a single soil profile for the entire sector results in poor average predictions and very high uncertainty.

3.2 Monitoring and modelling fluxes of water and nutrients to surface drainage network from irrigated fields

Coppola et al. (2024) coupled FLOWS to a Kinematic Wave-based code, named KWV, to study the fate of water and nutrient fluxes coming from agricultural fields in a

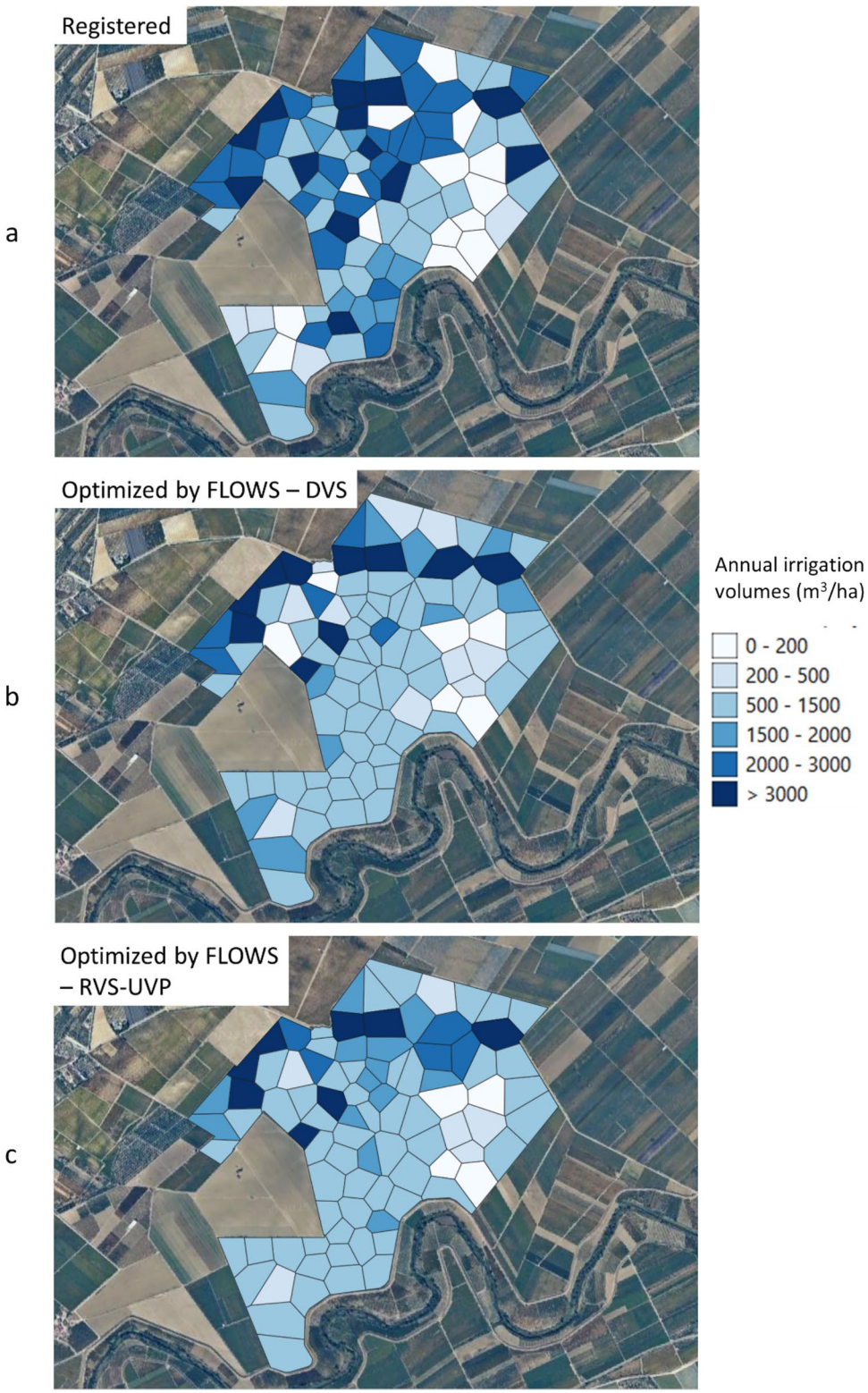


Fig. 13 Colour-graduated maps of the average irrigation volumes represented in m^3/ha as applied by the farmers (**a**) and as optimized by FLOWS according to the DVS (**b**). The legend on the right shows the colours corresponding to each irrigation volume interval

hydraulically reclaimed area. For this purpose, the study area was selected as a 16-ha experimental field in a the hydraulically reclaimed area of "Piana del Sassu" in Arborea area on the west coast of Sardinia Island, Italy. The experimental field consists of an upstream, UsF, and downstream, DsF, sub-fields (Fig. 15). In 2021, the UsF was cultivated with corn and the DsF was cultivated with melon. In 2022, both UsF and DsF were cultivated with corn.

As shown in Fig. 15, the experimental field is divided into small identical rectangular plots, each 25 m wide and

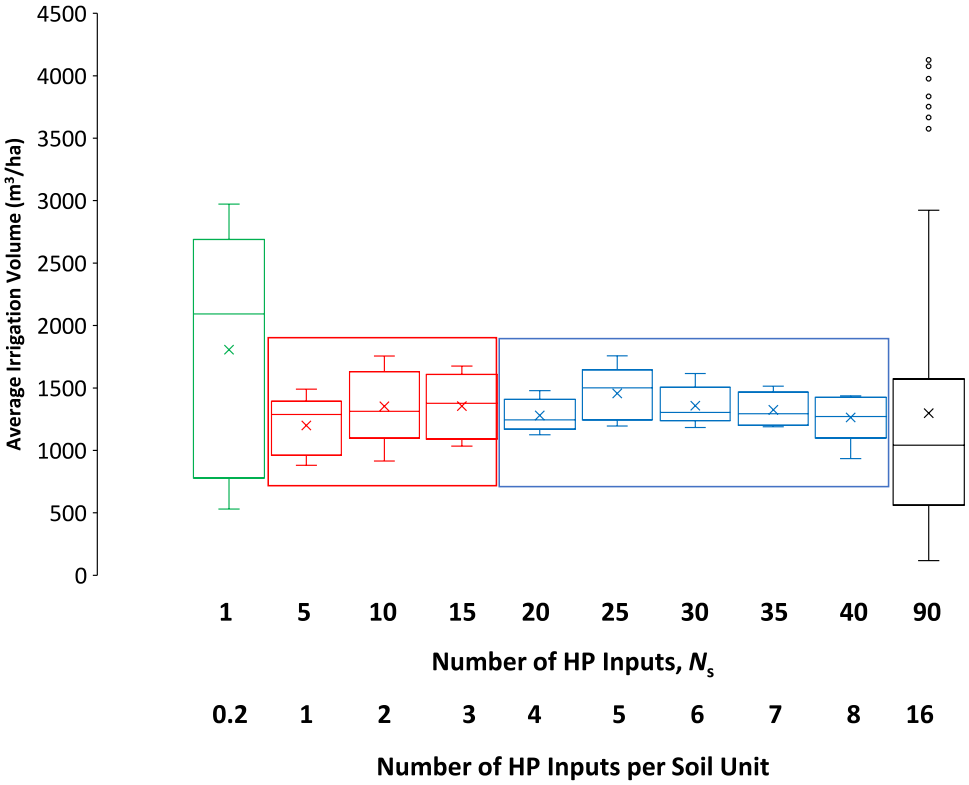


Fig. 14 Box plots corresponding to each number of HP input, N_s, including the weighted averages (symbols), the medians (horizontal lines), the minimum (lower whiskers), the maximum (upper whiskers) and the first and third quartiles (the boxes) of the average irrigation volumes. The box plot for the 90 sites refers to the deterministic scenario involving simulations carried out using spatially variable soil and vegetation properties (DVS)

200 m long. There is a ditch adjacent to each field to collect drainage water (the vertical blue lines in Fig. 15), each ditch is 200 m long. The ditches drain their water to a secondary drainage channel which drains its water to the main drainage canal.

In the study, four Monitoring Stations, MS, were installed in the field: two in UsF and two in DsF. Each MS was equipped with water content reflectometer sensors, multiparametric probes, water level sensors and tensiometers. The probes measure volumetric water contents, θ, bulk electrical conductivity, EC, and temperature.

Two triangular weirs were installed along the secondary drainage channel for measuring water discharges: upstream, us_weir, intercepting fluxes coming from the UsF and downstream, ds_weir, intercepting the total fluxes coming from the whole field. Close to each weir, a water level sensor was installed, along with a multiparametric probe, which provided measurements of standard water parameters (temperature, Dissolved Oxigen, Redox Potential, pH), as well as of nitrate concentrations measured by a nitrate ion-specific electrode. Additionally, phosphorus concentrations were also obtained from periodic sampling of channel water at the weir locations, with analyses performed using the photometric method.

A detailed soil hydrological characterization was conducted near each MS location. Pedological pits (approximately 1.5 × 1.5 × 1.5 m) were excavated near the installation points, with site selection guided by an existing pedological map of the Sassu plain. Two undisturbed samples were collected from each identified horizon down to about 1.5 m depth using stainless-steel cylinders, which were analyzed to provide bulk density and soil water retention and hydraulic conductivity curves (the soil HP). Soil water retention was described by unimodal van Genuchten model [43], and the hydraulic conductivity was described by Mualem model [44].

In this study, FLOWS was used for simulating water and nutrient balances, including water and solute fluxes to runoff caused by excess rainfall or irrigation, as well as to subsurface artificial drainage. Then, the KWV was used for routing runoff fluxes of water and dissolved nutrients in the overland flow, through ditches, from the ditches to the secondary drainage channel and eventually to the field outlet.

The top boundary conditions for FLOWS water flow simulations were set as variable fluxes to account for the measured precipitation and irrigation fluxes, as well as the potential evapotranspiration, ET_p. In addition, top boundary conditions for solute transport processes were set as the days and amounts of the applied nitrate- and phosphorus-based fertilizers in kg/ha. The bottom boundary condition for FLOWS simulations was set as a variable pressure head based on the tensiometer data. The solute transformation parameters were obtained from laboratory analyses.

For the KWV model simulations and related input parameters, see Coppola et al. [7].

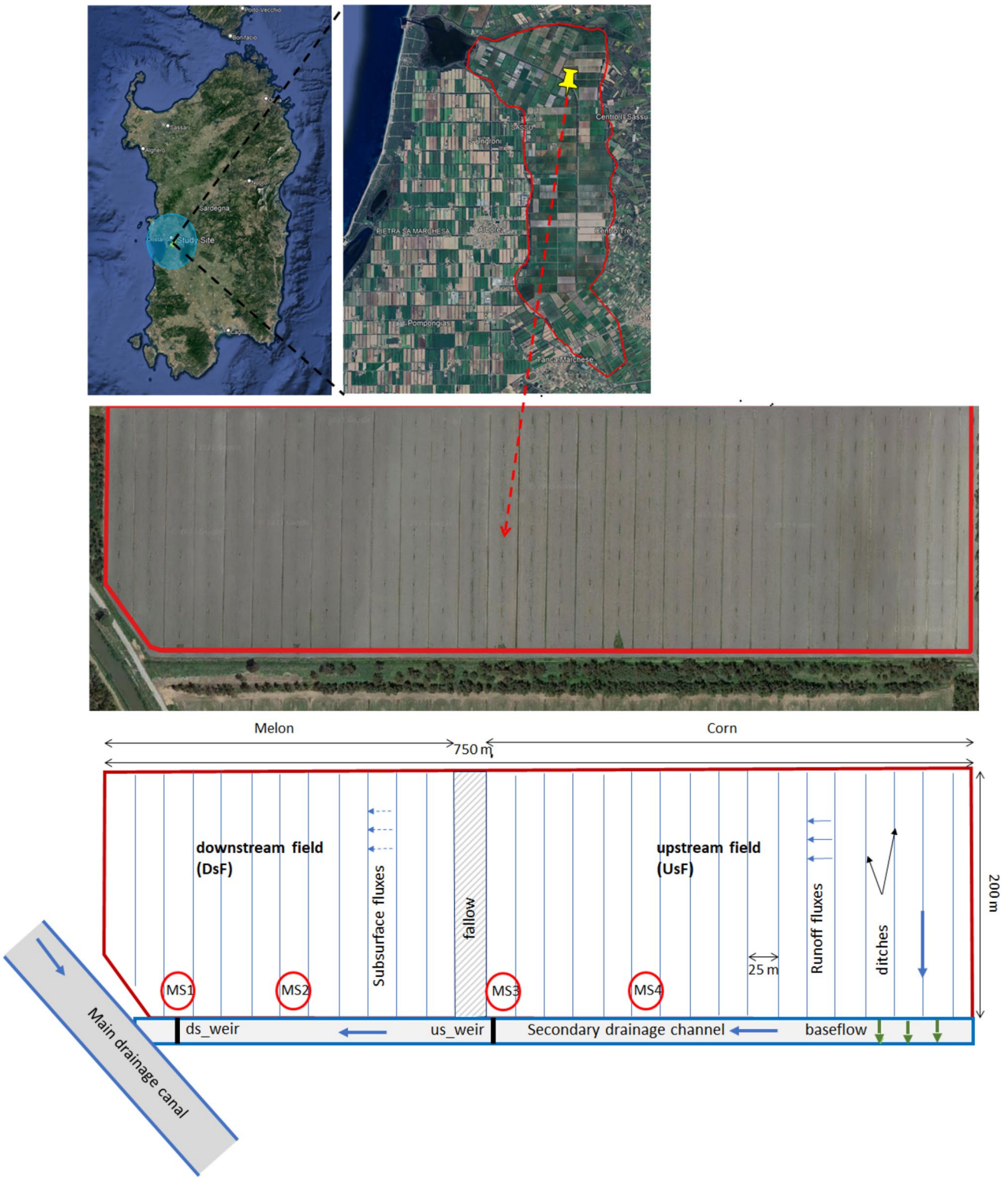


Fig. 15 From Coppola et al. [7], a map of the study area in "Piana del Sassu" (bordered by red lines) in Arborea Area, Sardinia Island, Italy. In the bottom right: a satellite image of the experimental field and its schematic view (not to scale). The field consists of two sub-fields: the upstream, UsF, and downstream, DsF, fields. The cropping pattern refers to 2021 while in 2022, UsF and DsF were cultivated with corn. MS refers to monitoring stations. Two triangular weirs were installed in the secondary channel for measuring water discharges: upstream, us_weir, and downstream, ds_weir. Green arrows represent the direction of the shallow groundwater contribution to water and solute fluxes towards the secondary channel. The blue vertical lines represent the ditches which are 25 m apart

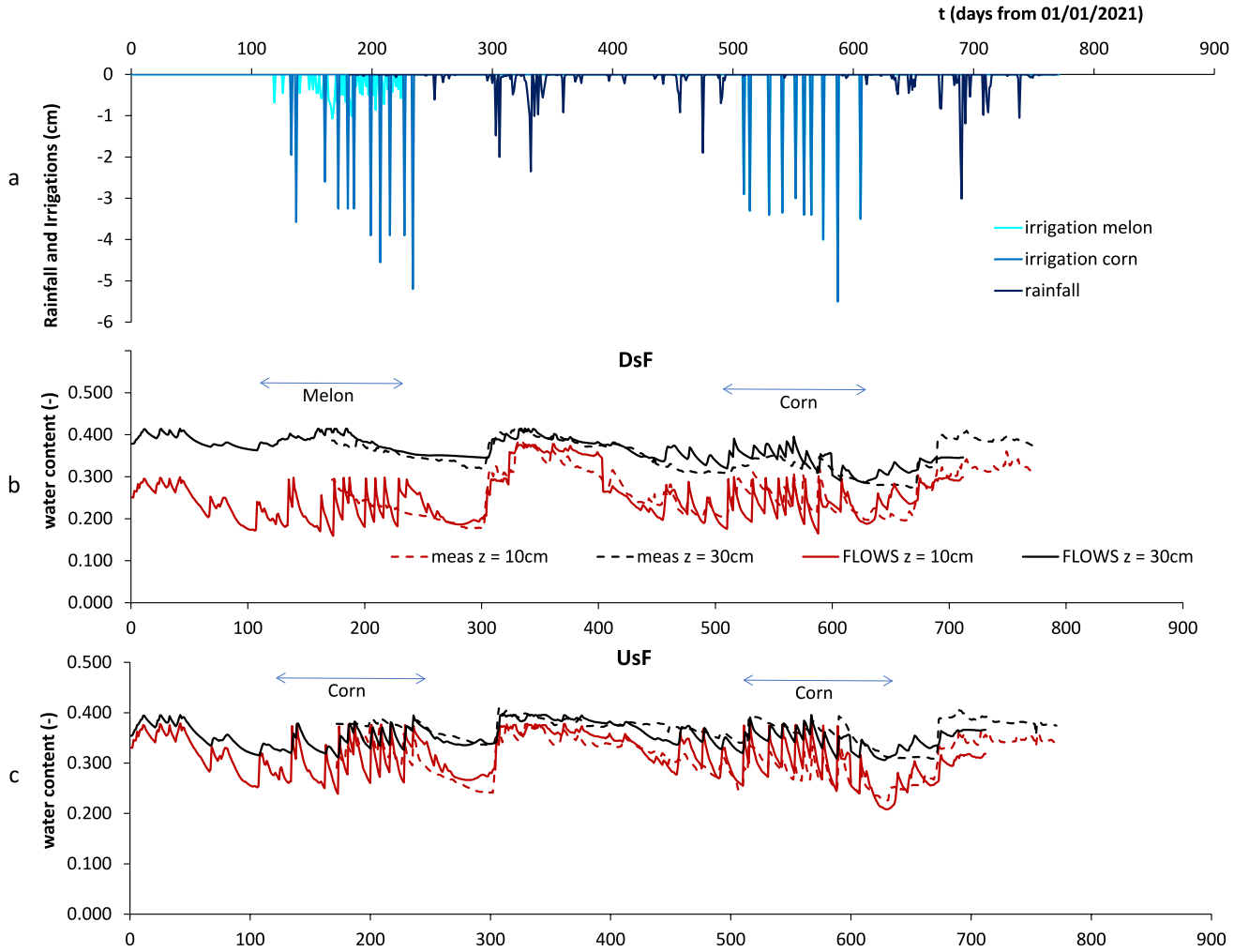


Fig. 16 From [7], the temporal evolution of the measured (symbols) and FLOWS-simulated (solid lines) soil water contents at different depths in the DsF (graph **b**) and the UsF (graph **c**). Graph (**a**) shows the temporal evolution of the measured precipitation and irrigation fluxes

The goodness of FLOWS simulations was evaluated by comparing FLOWS estimations of soil water content evolution with measured water contents at different depths, as well as coupled FLOWS-KWV estimations of water discharges and nutrients concentrations with water discharges, nitrate and phosphorus concentrations measured in the secondary drainage channel. The comparison was conducted for two consecutive years, 2021 and 2022.

Figure 16 shows the measured and FLOWS-simulated water contents in the UsF and DsF at depths of 10 cm and 30 cm. Simulations and measurements at the other observation depths are not shown for the sake of brevity, as they partly reflect the patterns already observed at the first two depths. The top panel of the figure shows the irrigation and precipitation fluxes, illustrating the response of soil water content to the top-boundary input fluxes.

Figure 16 shows the high sensitivity of the measurements to the input water fluxes (precipitation and irrigation), both at 10 and 30 cm depths, and that FLOWS largely reproduced the observed dynamics with good accuracy; the overall Root-Mean-Square Error, RMSE, values of the soil water contents at 10 and 30 cm were 0.079 and 0.045, respectively. In this sense, it should be noted that all simulations were conducted using FLOWS in a forward mode, without calibration, thus relying only on measured soil hydraulic properties, with upper boundary conditions defined by observed rainfall and irrigation inputs and lower boundary conditions prescribed from tensiometer measurements.

FLOWS also produced water and solute fluxes to runoff and to lateral drains in each of the plots in the UsF and DsF. An example of those fluxes is reported in Fig. 17. Specifically graph (a) reports the water fluxes to runoff in the UsF cultivated with corn (on the left Y-axis) and the subsurface lateral flow to drains in the DsF cultivated with melons (on the right Y-axis). Graphs (b), (c) and (d) report the N-NO_3 and P-PO_4 fluxes associated with the water fluxes in graph (a).

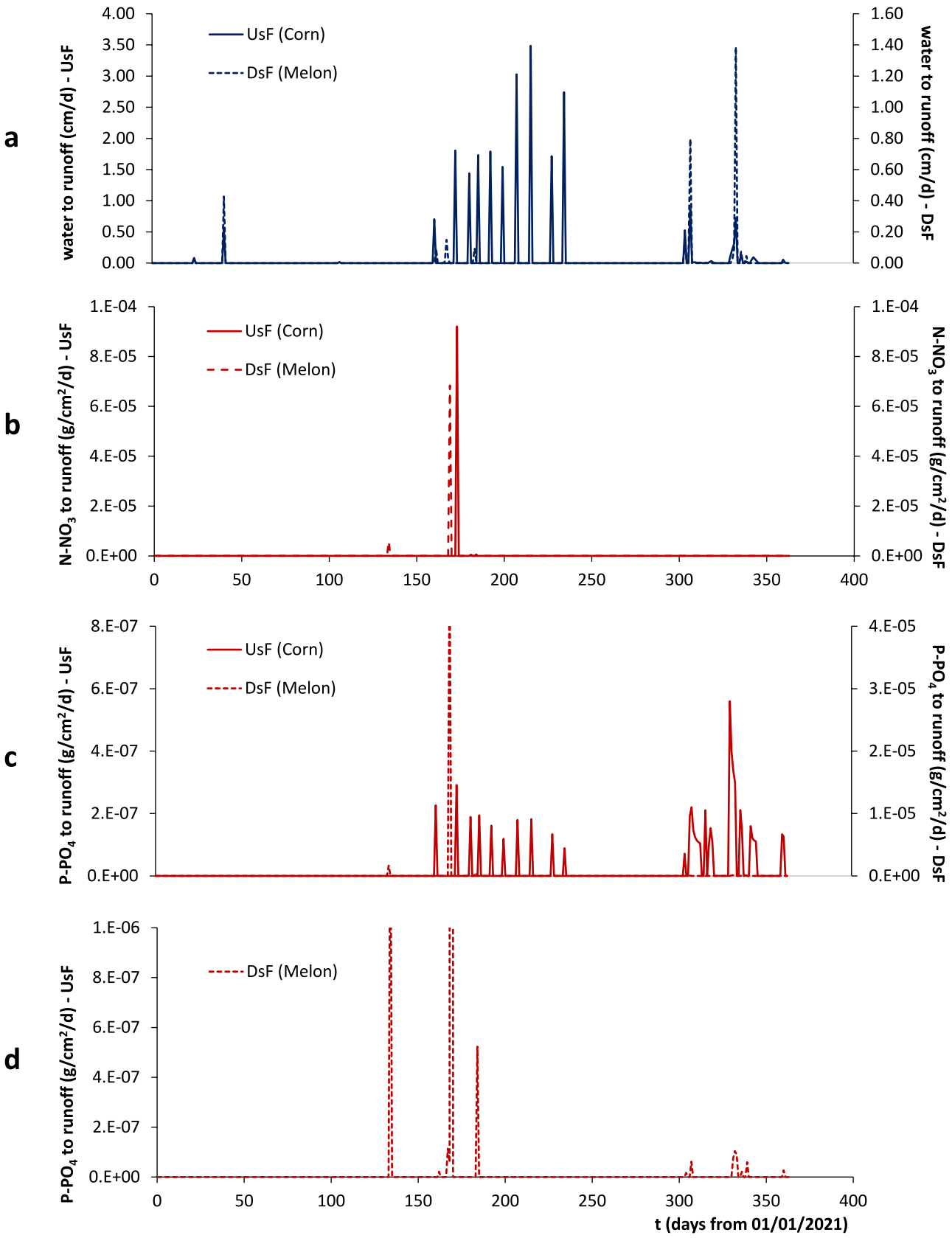

a
water to runoff (cm/d) - UsF
water to runoff (cm/d) - DsF
UsF (Corn)
DsF (Melon)
b
N-NO3 to runoff (g/cm²/d) - UsF
N-NO3 to runoff (g/cm²/d) - DsF
c
P-PO4 to runoff (g/cm²/d) - UsF
P-PO4 to runoff (g/cm²/d) - DsF
d
t (days from 01/01/2021)

Fig. 17 An example of water, N-NO_3 and P-PO_4 fluxes to runoff simulated by FLOWS for each plot in the UsF and DsF in the year 2021. Graph (**a**) shows reports the runoff water fluxes in the UsF (cultivated with corn) in solid blue lines and the lateral subsurface drainage to ditches in the DsF (cultivated with melon) in dashed blue lines. Graphs (**b**) and (**c**) report the N-NO_3 and P-PO_4 fluxes, respectively, in the UsF surface runoff (solid red lines) and in the DsF subsurface lateral drainage flow (dashed red lines). Graph (**d**) replicates the P-PO_4 fluxes in the DsF in graph (**c**) but with a rescaled Y-axis to show the peaks of P-PO_4 peak fluxes in the summer and winter periods, which are not visible in graph (**c**)

The water and solute fluxes to runoff and lateral drainage generated by the FLOWS model were used as inputs to the KWV model for flow routing. The KWV model produced simulated water and solute hydrographs, which were compared with observations collected along the secondary drainage channel. Specifically, comparisons were made at the control sections corresponding to the upstream weir (us_weir) installed at MS3 (Fig. 15), which captures water and solute fluxes originating solely from the UsF, and the downstream weir (ds_weir) located at MS1, which intercepts flows from both the UsF and DsF.

Figure 18 reports: 1) the runoff and subsurface lateral drainage water fluxes simulated by FLOWS (graphs a1 and a2); 2) the simulated water discharges and nitrate

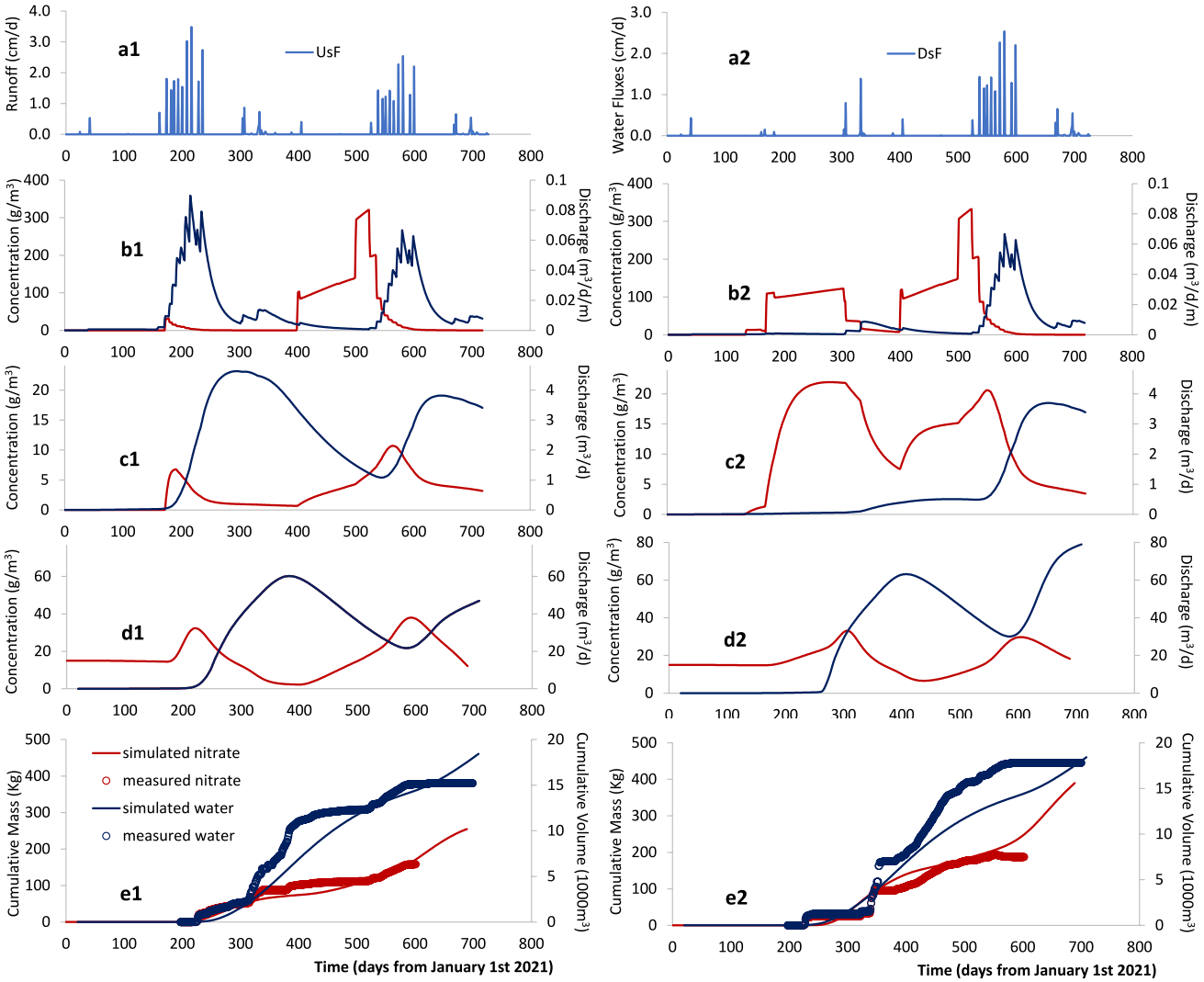


Fig. 18 From [7], the simulated water (blue) and nitrate (red) in surface runoff and subsurface lateral flows across the drainage network different compartments of the UsF and DsF for the 2021–2022 simulation period. Graph (**a1**): the FLOWS-simulated surface runoff fluxes in the UsF. Graph (**a2**): the FLOWS-simulated water fluxes in the DsF (subsurface lateral flow in 2021 and surface runoff in 2022). Graph (**b1**): the water discharge and nitrate concentration in overland flow in each elementary plot of the UsF. Graph (**b2**): water discharge and nitrate concentration in subsurface lateral flow in 2021 and overland flow in 2022 in each elementary plot of the DsF. Graphs (**c1**) and (**c2**): the water discharges and nitrate concentrations in each ditch. Graphs (**d1**) and (**d2**): the water discharges and nitrate concentrations in the secondary channel, specifically at the us_weir and ds_weir locations. Graphs (**e1**) and (**e2**): the simulated and measured cumulative water volumes and nitrate masses at the us_weir and the ds_weir, respectively

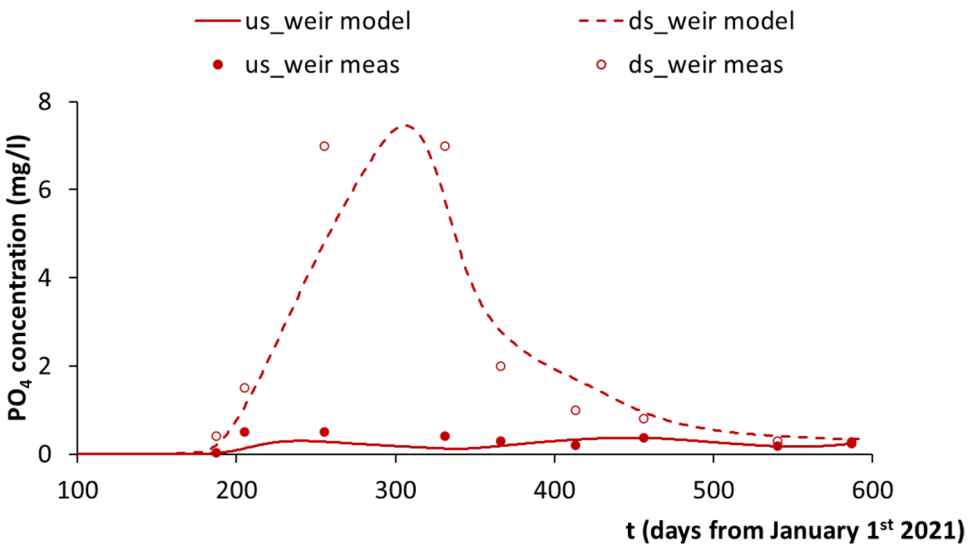


Fig. 19 The simulated (lines) and measured (symbols) PO_4 concentrations at the us_weir (solid lines and filled symbols)) and the ds_weir (dashed lines and hollow symbols)

concentrations in each elementary plot (graphs b1 and b2); 3) in each ditch (graphs c1 and c2) and 4) along the secondary drainage channel at the us_weir and ds_weir, respectively, (graphs d1 and d2). Finally, the cumulative simulated and measured water volumes and nitrate masses along the secondary drainage channel at the us_weir and the ds_weir are reported in graphs (e1) and (e2) compared to the measured values.

Figure 18 showcases the ability of integrating the physically based models FLOWS (for agrohydrological simulations) and KWV (for flood routing) to simulate water discharges and nutrient concentrations at different compartments in the complicated drainage network. Overall, as shown in Fig. 18 (e1) and 18 (e2), the model was largely able to reproduce the observed water volumes and nitrate masses conveyed through the secondary channel. The absolute difference between the simulated and measured final cumulative water volumes were 3210 and 190 m^3 at the upstream and downstream weirs, respectively. The absolute difference between the simulated and measured final cumulative nitrate masses were 12.54 and 60.08 kg at the upstream and downstream weirs, respectively. Finally, Fig. 19 shows that FLOWS was also able to provide accurate estimations of $P–PO_4$ concentrations, closely matching the measurements carried out at the weir locations.

4 Conclusions

FLOWS integrates the fundamental interacting processes that control water dynamics and nutrient transformation and transport through the unsaturated zone toward groundwater, as well as water and solute fluxes to surface waters via runoff and artificial drainage, under specific environmental conditions and agronomic management practices.

Compared to other existing Richards equation-based models, which build agro-hydrological decision support tools by sequentially coupling the hydrological model to other existing models dealing with nutrient and soil organic matter management, FLOWS has several distinctive features: (1) Integrated simulation of carbon, nitrogen, and phosphorus cycles, fully coupled with soil water content and fluxes; (2) Advanced irrigation management capabilities, allowing optimization of irrigation timing and volumes based on criteria related to the average pressure head in the root zone; and (3) Integrated simulation of water and solute transport to runoff and artificial drainage systems.

All processes are dynamically coupled with the hydrological component of the model. Soil water contents and fluxes, computed through the numerical solution of the Richards equation, serve as inputs to the carbon and nutrient transformation and transport modules at each time step. This ensures consistent, physically based interactions between water flow and solute dynamics.

As a result, FLOWS provides a powerful, physically based tool for identifying best agro-hydrological management practices, particularly with respect to irrigation and fertilizer management. The model supports optimization of water and nutrient use while minimizing nutrient—and more generally agrochemical—losses to water bodies.

The applications of FLOWS to real and complex agro-hydrological systems presented in this paper demonstrate that, when adequately supported by observations and detailed site characterization, the model can reliably identify site-specific optimal water and nutrient management strategies. In doing so, FLOWS contributes to the prevention of agricultural non-point source pollution by enabling more informed, site-specific decisions that explicitly account for ecohydrological impacts. Furthermore, the use of the model in a multisite configuration enables the optimization of

agro-hydrological management at operational scales, such as irrigation districts. Future research will include incorporating a crop growth module, based on EPIC model [45] and is currently under testing, so that the model simulates the temporal evolution of vegetation parameters rather than being inputs by the user.

Acknowledgements This work was supported by the PRIN 2022 project entitled "Monitoring and modelling of contaminants transport in soil across spatial scales", funded by the Italian Ministry of University and Research (MUR) – Prot. 20229FCFMM – CUP C53D23005140006

Author contributions A.C. (Coppola) developed the MATLAB code, wrote the main manuscript and performed the main analyses. A.B., A.C. (Comegna) and S.B.M.H tested the code and performed the code benchmarking. C.F. and A.C. (Concas) developed the desktop graphical interface. F.P. developed the web-based graphical interface. S.B.MH. also participated at writing the manuscript.

Funding Open access funding provided by Università degli Studi della Basilicata within the CRUI-CARE Agreement. This article was funded by Ministero dell'Università e della Ricerca, 20229FCFMM.

Data availability No datasets were generated or analysed during the current study.

Open Access This article is licensed under a Creative Commons Attribution 4.0 International License, which permits use, sharing, adaptation, distribution and reproduction in any medium or format, as long as you give appropriate credit to the original author(s) and the source, provide a link to the Creative Commons licence, and indicate if changes were made. The images or other third party material in this article are included in the article's Creative Commons licence, unless indicated otherwise in a credit line to the material. If material is not included in the article's Creative Commons licence and your intended use is not permitted by statutory regulation or exceeds the permitted use, you will need to obtain permission directly from the copyright holder. To view a copy of this licence, visit http://creativecommons.org/licenses/by/4.0/.

References

1. Power AG (2010) Ecosystem services and agriculture: tradeoffs and synergies. Philos Trans R Soc B Biol Sci 365:2959–2971. https://doi.org/10.1098/rstb.2010.0143
2. Kroes JG, Van Dam JC, Bartholomeus RP et al (2017) SWAP version 4. Wageningen Environmental Research
3. Gul K, Singh AK, Jabeen R (2016) Nutraceuticals and functional foods: the foods for the future world. Crit Rev Food Sci Nutr 56:2617–2627. https://doi.org/10.1080/10408398.2014.903384
4. Coppola A, Basile A, Comegna A et al (2026) FLOWS: a model to simulate water and solutes fluxes in agricultural and environmental systems. 1. Theory and applications with intercode benchmarking
5. Coppola A, Dragonetti G, Comegna A et al (2014) Mapping solute deep percolation fluxes at regional scale by integrating a process-based vadose zone model in a Monte Carlo approach. Soil Sci Plant Nutr 60:71–91. https://doi.org/10.1080/00380768.2013.855615
6. Coppola A, Dragonetti G, Sengouga A et al (2019) Identifying optimal irrigation water needs at district scale by using a physically based agro-hydrological model. Water. https://doi.org/10.3390/w11040841
7. Coppola A, Zucaro R, Baralla S et al (2024) Monitoring and modelling fluxes of water and nutrients to surface drainage network from irrigated agricultural fields in a hydraulically reclaimed coastal area. Ecohydrology 17:e2723. https://doi.org/10.1002/eco.2723
8. Porru MC, Hassan SBM, Abdelmaqsoud MSM et al (2024) Using index and physically-based models to evaluate the intrinsic groundwater vulnerability to non-point source pollutants in an agricultural area in Sardinia (Italy). Front Water. https://doi.org/10.3389/frwa.2024.1399170
9. Fusco F, Allocca V, Bancheri M et al (2024) A multi-method approach for assessing groundwater vulnerability of shallow aquifers in the Marchfeld region (Austria). J Hydrol Reg Stud 54:101865. https://doi.org/10.1016/j.ejrh.2024.101865
10. Hassan SBM, Dragonetti G, Comegna A et al (2024) Analyzing the role of soil and vegetation spatial variability in modelling hydrological processes for irrigation optimization at large scale. Irrig Sci. https://doi.org/10.1007/s00271-023-00882-7
11. Alla A, Berardi M, Saluzzi L (2025) State dependent Riccati for dynamic boundary control to optimize irrigation in Richards' equation framework. Math Comput Simul 232:261–275. https://doi.org/10.1016/j.matcom.2024.12.020
12. Mao Y, Liu S, Nahar J et al (2018) Soil moisture regulation of agro-hydrological systems using zone model predictive control. Comput Electron Agric 154:239–247. https://doi.org/10.1016/j.compag.2018.09.011
13. Holmes TRH, Owe M, De Jeu RAM, Kooi H (2008) Estimating the soil temperature profile from a single depth observation: a simple empirical heatflow solution. Water Resour Res. https://doi.org/10.1029/2007WR005994
14. Van Wijk WR, De Vries DA (1963) Periodic temperature variations in a homogeneous soil. Phys Plant Environ 1:103–143
15. Elias EA, Cichota R, Torriani HH, de Jong van Lier Q (2004) Analytical soil–temperature model. Soil Sci Soc Am J 68:784–788. https://doi.org/10.2136/sssaj2004.7840
16. Horton R, Aguirre-Luna O, Wierenga PJ (1984) Soil temperature in a row crop with incomplete surface cover. Soil Sci Soc Am J 48:1225–1232. https://doi.org/10.2136/sssaj1984.03615995004800060004x
17. Milly PCD (1982) Moisture and heat transport in hysteretic, inhomogeneous porous media: a matric head-based formulation and a numerical model. Water Resour Res 18:489–498. https://doi.org/10.1029/WR018i003p00489
18. Hanks RJ, Austin DD, Ondrechen WT (1971) Soil temperature estimation by a numerical method. Soil Sci Soc Am J 35:665–667. https://doi.org/10.2136/sssaj1971.03615995003500050015x
19. Wierenga PJ, de Wit CT (1970) Simulation of heat transfer in soils. Soil Sci Soc Am J 34:845–848. https://doi.org/10.2136/sssaj1970.03615995003400060012x
20. Jury WA, Spencer WF, Farmer WJ (1983) Behavior assessment model for trace organics in soil: I. Model description. J Environ Qual 12:558–564. https://doi.org/10.2134/jeq1983.00472425001200040025x
21. Stanford G, Smith SJ (1972) Nitrogen mineralization potentials of soils. Soil Sci Soc Am J 36:465–472. https://doi.org/10.2136/sssaj1972.03615995003600030029x
22. Watts DG, Hanks RJ (1978) A soil-water-nitrogen model for irrigated corn on sandy soils. Soil Sci Soc Am J 42:492–499. https://doi.org/10.2136/sssaj1978.03615995004200030024x

23. Kersebaum KC, Richter J (1991) Modelling nitrogen dynamics in a plant-soil system with a simple model for advisory purposes. Fertil Res 27:273–281. https://doi.org/10.1007/BF01051133
24. Gusman JA, Mariño MA (1999) Analytical modeling of nitrogen dynamics in soils and ground water. J Irrig Drain Eng 125:330–337. https://doi.org/10.1061/(ASCE)0733-9437(1999)125:6(330)
25. Williams JR, Renard KG, Dyke PT (1983) EPIC: a new method for assessing erosion's effect on soil productivity. J Soil Water Conserv 38:381–383
26. Jones CA, Cole CV, Sharpley AN, Williams JR (1984) A simplified soil and plant phosphorus model: I. Documentation. Soil Sci Soc Am J 48:800–805. https://doi.org/10.2136/sssaj1984.03615995004800040020x
27. Šimůnek J, Suarez DL (1993) Modeling of carbon dioxide transport and production in soil: 1. Model development. Water Resour Res 29:487–497. https://doi.org/10.1029/92WR02225
28. Spohn M, Klaus K, Wanek W, Richter A (2016) Microbial carbon use efficiency and biomass turnover times depending on soil depth—implications for carbon cycling. Soil Biol Biochem 96:74–81. https://doi.org/10.1016/j.soilbio.2016.01.016
29. Sander R (2015) Compilation of Henry's law constants (version 4.0) for water as solvent. Atmos Chem Phys 15:4399–4981. https://doi.org/10.5194/acp-15-4399-2015
30. Cleveland CC, Liptzin D (2007) C:N:P stoichiometry in soil: is there a "Redfield ratio" for the microbial biomass? Biogeochemistry 85:235–252. https://doi.org/10.1007/s10533-007-9132-0
31. Spohn M (2015) Microbial respiration per unit microbial biomass depends on litter layer carbon-to-nitrogen ratio. Biogeosciences 12:817–823. https://doi.org/10.5194/bg-12-817-2015
32. Liang XQ, Chen YX, Li H et al (2007) Modeling transport and fate of nitrogen from urea applied to a near-trench paddy field. Environ Pollut 150:313–320. https://doi.org/10.1016/j.envpol.2007.02.003
33. Cabon F, Girard G, Ledoux E (1991) Modelling of the nitrogen cycle in farm land areas. Fertil Res 27:161–169. https://doi.org/10.1007/BF01051124
34. Lafolie F (1991) Modelling water flow, nitrogen transport and root uptake including physical non-equilibrium and optimization of the root water potential. Fertil Res 27:215–231. https://doi.org/10.1007/BF01051129
35. McGechan MB, Wu L (2001) A review of carbon and nitrogen processes in European soil nitrogen dynamics models. In: Shaffer MJ, Ma L, Hansen S (eds) Modelling carbon and nitrogen dynamics for soil management. Lewis publishers, Boca Raton, pp 103–171
36. van Dam JC, Huygen J, Wesseling JG et al (1997) Theory of SWAP version 2.0; simulation of water flow, solute transport and plant growth in the soil-water-atmosphere-plant environment. DLO Winand Staring Centre
37. Mansell RS, Selim HM, Fiskell JGA (1977) Simulated transformations and transport of phosphorus in soil. Soil Sci 124
38. Mansell RS, Selim HM, Kanchanasut P et al (1977) Experimental and simulated transport of phosphorus through sandy soils. Water Resour Res 13:189–194. https://doi.org/10.1029/WR013i001p00189
39. Barrow NJ, Madrid L, Posner AM (1981) A partial model for the rate of adsorption and desorption of phosphate by goethite. J Soil Sci 32:399–408. https://doi.org/10.1111/j.1365-2389.1981.tb01715.x
40. Van Der Zee SEATM, Van Riemsdijk WH (1986) Sorption kinetics and transport of phosphate in sandy soil. Geoderma 38:293–309. https://doi.org/10.1016/0016-7061(86)90022-4
41. Coppola A, Hassan SBM, Pili F (2025) FLOWS - FLOw of water and solutes in agricultural and environmental systems (WEB version 1.0). Zenodo. https://doi.org/10.5281/zenodo.17076523
42. Jarvis N, Larsbo M, Lewan E, Garré S (2022) Improved descriptions of soil hydrology in crop models: the elephant in the room? Agric Syst 202:103477. https://doi.org/10.1016/j.agsy.2022.103477
43. van Genuchten MTH (1980) A closed-form equation for predicting the hydraulic conductivity of unsaturated soils. Soil Sci Soc Am J 44:892–898. https://doi.org/10.2136/sssaj1980.03615995004400050002x
44. Mualem Y (1976) A new model for predicting the hydraulic conductivity of unsaturated porous media. Water Resour Res 12(3):513–522. https://doi.org/10.1029/WR012i003p00513 https://doi.org/10.1029/WR012i003p00513
45. Williams RJ, Jones AC, Kiniry RJ, Spanel AD (1989) The EPIC crop growth model. Trans ASAE 32:497–511. https://doi.org/10.13031/2013.31032

Publisher's Note Springer Nature remains neutral with regard to jurisdictional claims in published maps and institutional affiliations.